# Chapter 1.   Introduction

## 1-1.   Photonic Crystals

In early twenty century, physicists found that electron in crystal scatter by lattice periodic potential, and energy gap arises in some wavelength by destructive interference causing band distribution dispersion relation, which is known as electronic band structure.

In 1987, E. Yablonovitch and S. John addressed electromagnetic wave in periodic dielectric can behave as electron in crystal and the optical characteristic is controlled by dielectric constant and spacial distribution of periodic structure[1]. The artificial material is called Photonic Crystal. The defining feature of a photonic crystal is the periodicity of dielectric material along one or more axes. Thereby photonic crystal can be divided into one-dimensional, two-dimensional and three-dimensional photonic crystal as shown in Fig. 1-1[2]. In my thesis, two-dimensional photonic crystal will be concerntrated.
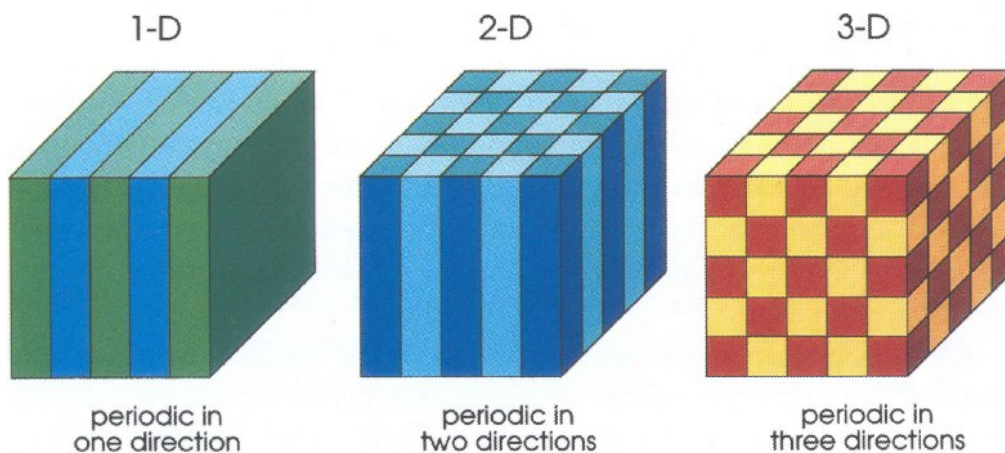


**Fig. 1-1.**    Simple examples of one-, two-, three-dimensional photonic crystals. The different colors represent materials with different dielectric constants.[1]

In order to explore photonic crystal band structure, electronic band theory is utilized. In periodically arranged crystal structure, the behavior of electron will observe Schrodinger equation :

$$[-\frac{\hbar^2}{2m^*}\nabla^2 + V(r)]\psi(r) = E\psi(r)$$ (1.1)

$m^*$ : **effective mass of electron**          $V(r)$ : **potential function**

$E$ : **eigen-energy**          $\psi(r)$ : **wavefunction**

The square of $\psi(r)$ denotes the probability density of electrons in space. When $\psi(r)$ term is equal to zero, i.e. there is no electron in some energy levels. These energy levels form the well-known electronic band gap. If the potential function is strong enough, the gap might extend to all directions, resulting in a "complete band-gap".

The behavior of light in photonic crystal can be regarded as the behavior of electron in crystal. The periodic refractive index provides potential function which is analogous to potential function of crystal to affect the behavior of light in photonic crystal. The motion of light in photonic crystal is described by Maxwell equations. By Maxwell equations, the master equation can be derived :

$$\nabla \times (\frac{1}{\varepsilon(r)}\nabla \times H(r)) = (\frac{w}{c})^2 H(r)$$ (1.2)

$\varepsilon(r)$ : **the dielectric constant variation function in space.**

$W$   : **frequency**          $C$ : **light velocity in vacuum**

$H(r)$ : **eigen-vector**

For a given $\varepsilon(r)$, we can solve the master equation to find the modes $H(r)$ for a given frequency. Thereby, these eigen-values and the corresponding eigen-vectors can be obtained. Then the band diagrams of photonic crystals can be also obtained.

H(r) term in some frequencies exponentially decay, and these frequencies form a forbidden in which light could not propagate. The frequency zone is so-called photonic band

gap. For example, we calculate the band diagram of two-dimensional photonic crystals with 500(nm) lattice constant and 150(nm) radius of air hole through two-dimensional plane-wave-expansion (PWE) method as shown in Fig. 1-2 and the two-dimensional triangular lattice photonic crystal is shown in inset. The index of InGaAsP is 3.4. In figure, the x-axis and y-axis denote the wave vector and normalized frequency a/$\lambda$. There are no eigen-values in the shadow region, i.e. light propagating in this region is forbidden in the triangular lattice photonic crystal. The shadow region is called "photonic band gap".
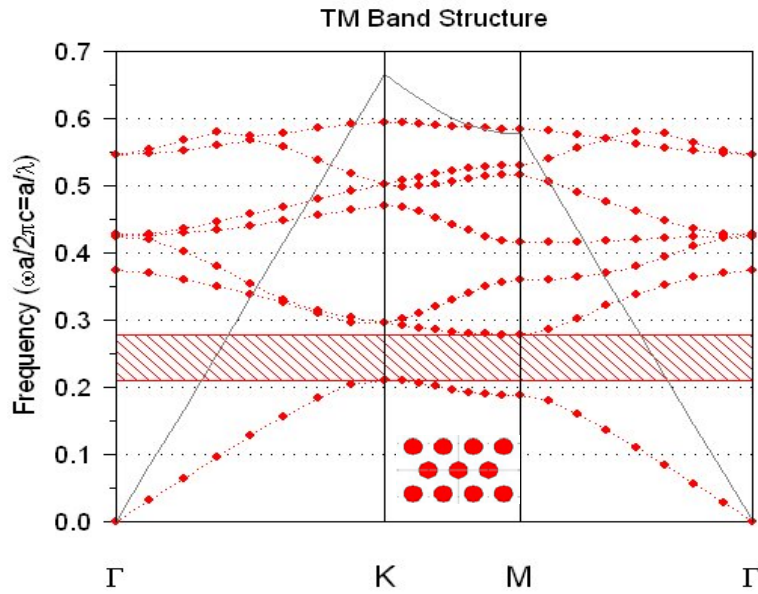


**Fig. 1-2.**    This is TM band diagram of two-dimensional triangular lattice photonic crystal. "TM" denotes light with electric field in the plane of crystal. There is a photonic band gap between the first band (known as dielectric band) and the second band (known as air band).

By utilizing photonic band gap effect, some defects by removing parts of the periodic structure in photonic crystal were constructed. Thereby, light in specific frequencies can propagate with low loss in defect region and is forbidden in photonic crystal region. In Fig. 1-3(a), a point defect is formed by removing a single air hole in two-dimensional photonic crystal slab. This is widely utilized to construct the photonic crystal cavities. In Fig. 1-3(b), a line defect os formed by removing one row of air holes in two-dimensional photonic crystal slab. This is widely utilized to construct low-loss photonic crystal waveguides.
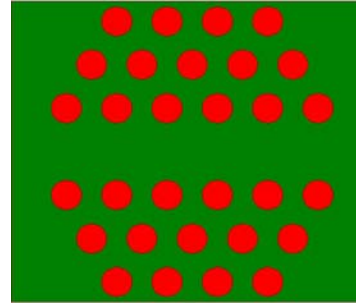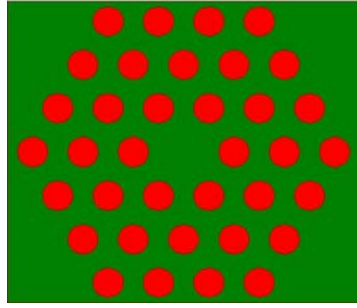
**Fig. 1-3.**         **(a) Point defect**                    **(b) Line defect**

## 1-2.    Developments of Photonic Crystal Lasers

On optical communication, laser source at long wavelength plays an important role. The characteristic of vertical cavity surface emitting laser (VCSEL) at optical communication wavelength (1550nm) is unable to accomplish ultra small cavity mode volume, low threshold current and high quality factor. However, photonic crystal laser is able to overcome difficulties above.

Presently, several groups play decisive roles in the filed of photonic crystal lasers, including O. Painter, A. Scherer, A. Yariv et al. at Caltech, J. D. O'Brien et al. at USC, S. Noda et al. at Kyoto University, and Y. H. Lee at KAIST. Recently, several important achievements were presented by these groups. Photonic crystal lasers can be divided into two categories which are photonic crystal cavity laser and photonic crystal band edge laser.

## 1-2-1.   Photonic Crystal Cavity Lasers

Utilizing photonic crystal to be reflected mirror around the cavity of laser was first proposed in 1994[3]. In 1999, two-dimensional photonic crystal lasers were first

demonstrated by O. Painter et al. at Caltech [4]. The typical configuration of a two-dimensional photonic crystal laser is shown in Fig. 1-4 [4].
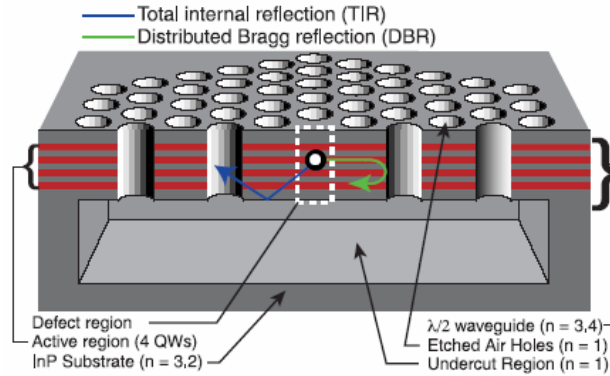


**Fig. 1-4.**    The typical structure of two-dimensional photonic crystal laser. [4]

In Fig. 1-4, the photonic crystal patterns are defined on two-dimensional dielectric slab with quantum wells or quantum dots through electron-beam lithography. Micro-cavity is formed by several missing air holes in photonic crystal patterns. Then undercut is fabricated for a symmetric waveguide structure. The photonic crystal patterns defined at active layers through the defect region construct photonic crystal micro-cavity. In the structure, a symmetric waveguide structure provides the vertical confinement by total reflection and the photonic crystal patterns provide the in-plane confinement by photonic band gap.

After first photonic crystal laser was presented, most researches focus on preferable characteristics of two-dimensional photonic crystal lasers, such as ultra-low threshold, high quality factor, high side mode suppression ratio, and small mode volume.

In 2002, O. Painter et al modified the size and the position of air holes around cavity in order to control the defect mode as shown in Fig. 1-5[5]. Because of altering effective refraction index in some direction by modulating air holes around cavity in the direction, the resonant mode in the direction is suppressed.
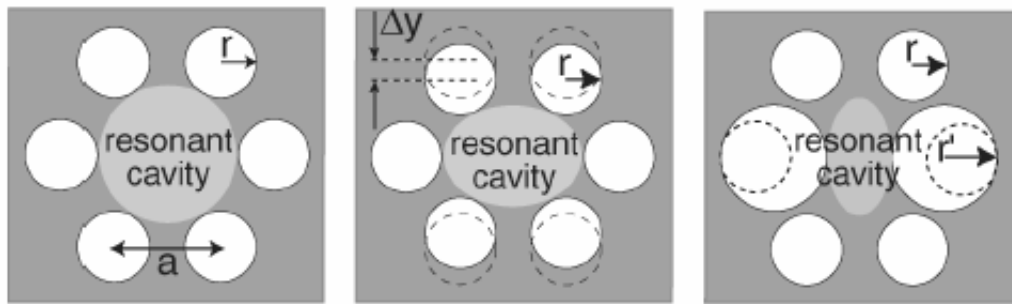
**Fig. 1-5.** Photonic crystal cavity geometries with different symmetries. [5]

In 2005, J. D. O'Brien et al added six smaller air holes in cavity destroys other resonant mode and preserves lasing mode. And then the side mode suppression ratio increases almost 10dB as shown in Fig. 1-6[6].
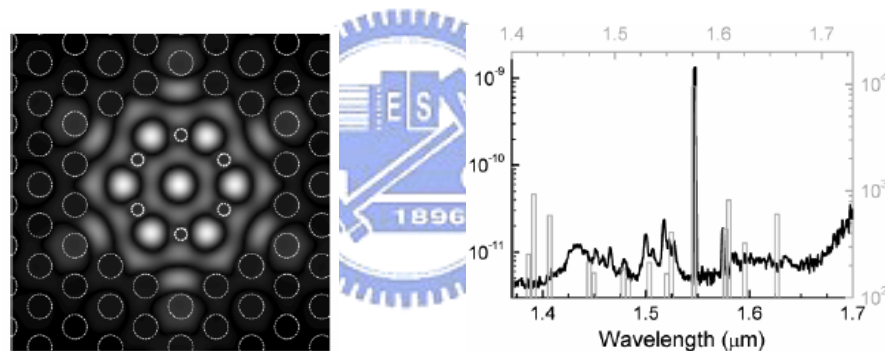


**Fig. 1-6.** Six smaller air holes are added to increase side mode suppression ratio. [6]

In 2004, the electrical pumping single defect photonic crystal micro-cavity laser with higher quality factor and lower threshold current than general VCSELs were demonstrated by H. G. Park and Y. H. Lee et al[7]. The schematic device is shown in Fig. 1-7(a). The small central post function as an electrical wire, a mode selector, and a heat sinker. And the L-I curve is shown in Fig. 1-7(b). This is a well proof of photonic crystal lasers with high quality factor and low threshold.
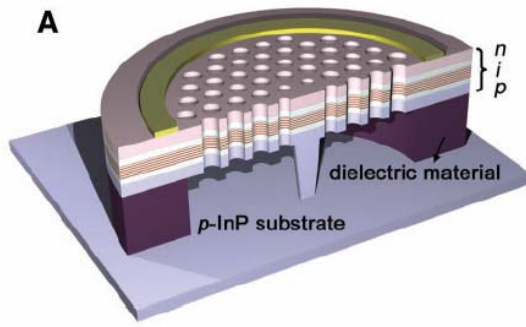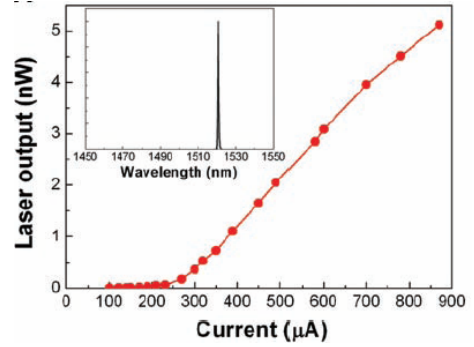
(a)                                        (b)

**Fig. 1-7.**   (a) The illustration of electrical pumping single defect photonic crystal

micro-cavity. (b) The L-I curve of this photonic crystal laser. [7]


## 1-2-2.   Photonic Crystal Band Edge Lasers


Because the slope of band is proportioned to the general definition of the group velocity: $V\mathbf{g} = dw\,/\,dk$, it will approach to zero near the photonic band-edge as shown in Fig1-8 simulated through two-dimensional plane-wave-expansion (PWE) method. This implies a longer optical path length in the photonic structure. If an active medium is present, longer optical path leads to better optical gain.
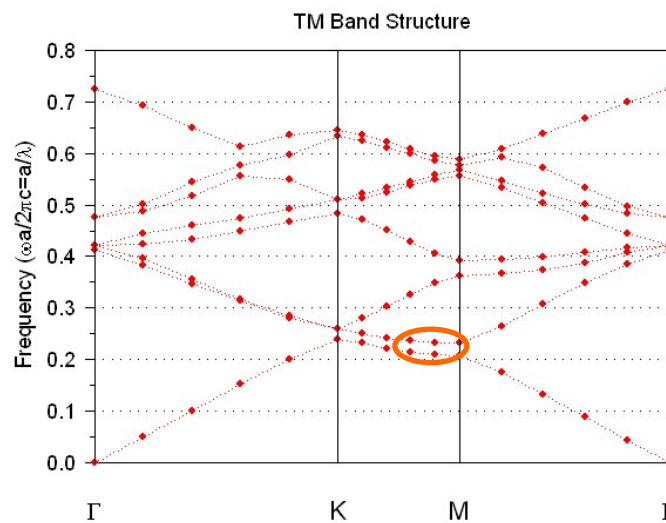


**Fig 1-8.**     The photonic band edge effect occurs in the circle.

If gain medium were present, the largely increasing in optical path length would enhance the effective gain. The smaller group velocity v**g** leads to a an increased optical path length l**eff** that is larger than the expected value l. The effective gain g**eff** can be estimated by：

$$g_{eff} / g \equiv l_{eff} / l = cn_2 / v_g \qquad (1.3)$$

At the band edge the group velocity is almost zero, i.e. effective gain will approach infinity.

In 1999, the photonic crystal band edge laser was first demonstrated by S. Noda et al. The photonic crystal is integrated with an multiple-quantum-well active layer by a wafer fusion technique as shown in Fig. 1-9[8]. The photonic band edge lasers has higher output power and narrower divergence angle than the photonic crystal cavity lasers.
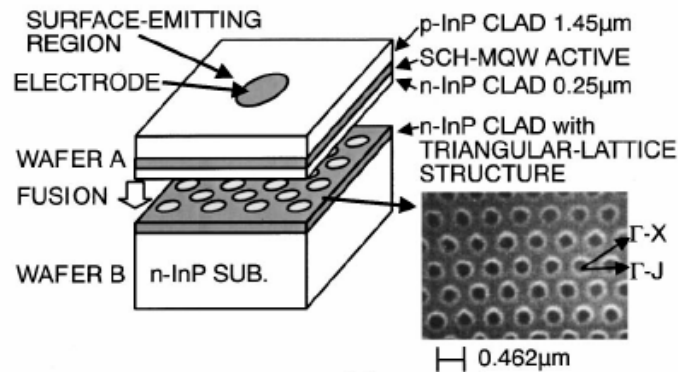


**Fig. 1-9.** Schematic structure of the surface-emitting laser has 2D triangular-lattice structure embedded by the wafer fusion technique. The inset shows the SEM photograph of the triangular-lattice structure. [8]

The type of photonic crystal device is not designed by photonic band gap effect, so the in-plane loss is larger than the photonic crystal cavity laser. In 2003, the graded structure was demonstrated to improve the in-plane loss by O. Painter et al as shown in Fig 1-10(a)[9]. And the L-L curve and sub-threshold spectrum is shown in Fig 1-10(b) [9].By utilizing in-plane

graded reflection index provides in-plane confinement like hetero-structure to suppress in-plane loss. The high quality factor will be achieved.
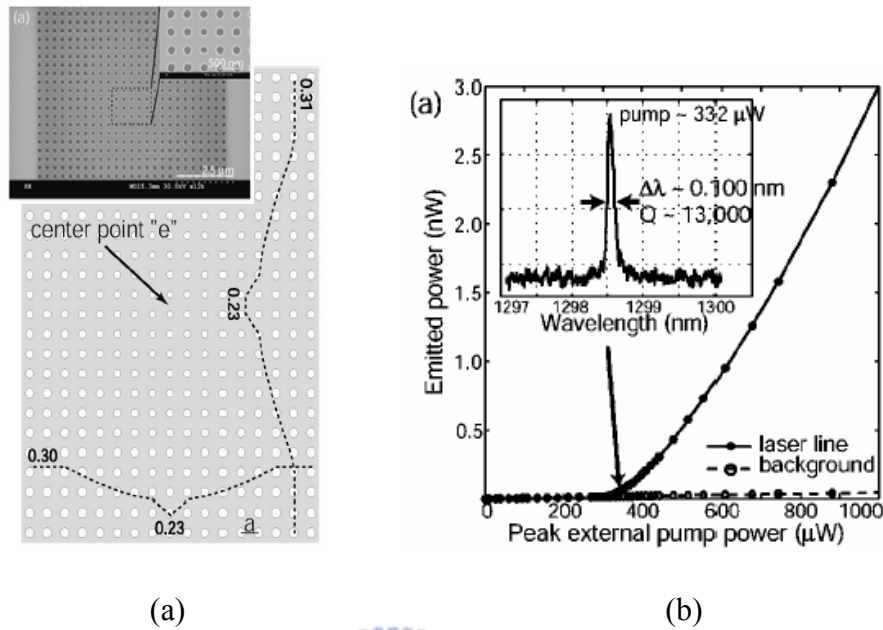


(a)                                    (b)

**Fig. 1-10.**    (a) Schematic graded structure. The inset shows the SEM photograph.

(b) The L-L curve of this photonic crystal band edge laser. [9]

Two-dimensional photonic crystal lasers are very attractive device for optical communication system. Many fabrications, simulation tools, and measurement system have been setup in order to gain lasers with high quality factor, low threshold, and small mode volume.


## 1-3.    Thesis Overview


In my thesis, the simulation, fabrication, measurement, and analysis of two-dimensional photonic crystal lasers are investigated. In chapter 2, the method of the simulation will be illustrated. In chapter 3, the photonic crystal laser design and simulation results will be embraced. In chapter 4, the fabrication and the measured results by NIR micro-photo-luminescence (PL) of two-dimensional circular photonic crystal lasers will be introduced. In chapter 5, the final conclusion will be presented.

# Chapter 2. Simulation Methods

## 2-1. Introduction

In this chapter, the numerical method to calculating the characteristic of photonic crystal will be illustrated. We solve the eigenvalue problem of the wave equation to calculate the photonic bands through plane wave expansion (PWE) method. And, we simulate the behavior of electromagnetic wave in the photonic crystal through finite-difference time-domain (FDTD) method. These numerical methods are very helpful to design the photonic crystal micro-cavity.

## 2-2. Plane-Wave Expansion Method

We begin with Maxwell's equations. Because we are interested the eigen-modes of the electromagnetic field and the interaction between the field, we assume that free charges and the electric current are absent. Maxwell's equations in the most general form are given in MKS units as following :

$$\nabla \times \vec{E}(\vec{r},t) = -\frac{\partial}{\partial t}\vec{B}(\vec{r},t) \tag{2.1}$$

$$\nabla \times \vec{H}(\vec{r},t) = \frac{\partial}{\partial t}\vec{D}(\vec{r},t) \tag{2.2}$$

$$\nabla \cdot \vec{D}(\vec{r},t) = 0 \tag{2.3}$$

$$\nabla \cdot \vec{B}(\vec{r},t) = 0 \tag{2.4}$$

Where E and H denote the electric and the magnetic field, D denotes the electric displacement, and B magnetic induction.

To solve the wave equations derived from Maxwell's equation, we need the constitutive equations that relate D to E and B to H. We assume that the magnetic permeability of photonic crystal is equal to that in free space, $\mu_0$. For the dielectric constant, we assume it is real, isotropic, perfectly periodic with respect to the spatial coordinate $\vec{r}$, and does not depend on frequency. We denote the dielectric constant in free space by $\varepsilon_0$ and the relative dielectric constant in the photonic crystal by $\varepsilon(\vec{r})$. Then, we obtained :

$$\vec{B}(\vec{r},t) = \mu_0 \vec{H}(\vec{r},t) \tag{2.5}$$

$$\vec{D}(\vec{r},t) = \varepsilon_0 \varepsilon(\vec{r})\vec{E}(\vec{r},t) \tag{2.6}$$

Since the dielectric constant is periodic distribution in photonic crystal, the periodicity of $\varepsilon(\vec{r})$ implies :

$$\varepsilon(\vec{r}+\vec{a}_i) = \varepsilon(\vec{r}) \qquad \text{(i=1, 2, 3)} \tag{2.7}$$
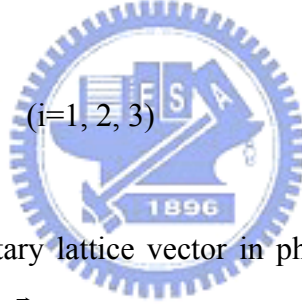
where $\vec{a}_i$ denotes the elementary lattice vector in photonic crystal. Because of this spatial periodicity, we can expand $\varepsilon^{-1}(\vec{r})$ in a Fourier series. For this, we introduce the elementary reciprocal lattice vectors $\{\vec{b}_i \ where \ i = 1,2,3\}$ and the reciprocal lattice vectors, $\{\vec{G}\}$ :

$$\vec{G} = l_1\vec{b}_1 + l_2\vec{b}_2 + l_3\vec{b}_3 \tag{2.8}$$

$$\vec{a}_i \cdot \vec{b}_j = 2\pi\delta_{ij} \tag{2.9}$$

where $l_i$ are arbitrary integers and $\delta_{ij}$ is Kronecker's delta. Then, $\varepsilon^{-1}(\vec{r})$ is expressed as :

$$\frac{1}{\varepsilon(\vec{r})} = \sum_{\vec{G}} \kappa(\vec{G})\exp(i\vec{G}\cdot\vec{r}) \tag{2.10}$$

Because we assumed that the dielectric constant is real, we obtained $\kappa(-\vec{G}) = \kappa^*(\vec{G})$.

11

When we substitute (2.5) and (2.6) into (2.1) ~ (2.4) and eliminate $\overline{E}(\vec{r},t)$ or $\overline{H}(\vec{r},t)$ , we obtain the following wave equations:

$$\frac{1}{\varepsilon(\vec{r})}\nabla \times \{\nabla \times \overline{E}(\vec{r},t)\} = -\frac{1}{c^2}\frac{\partial^2}{\partial t^2}\overline{E}(\vec{r},t) \tag{2.11}$$

$$\nabla \times \{\frac{1}{\varepsilon(\vec{r})}\nabla \times \overline{H}(\vec{r},t)\} = -\frac{1}{c^2}\frac{\partial^2}{\partial t^2}\overline{H}(\vec{r},t) \tag{2.12}$$

where c denotes the light velocity in free space, and c is equal to $\dfrac{1}{\sqrt{\varepsilon_0 \mu_0}}$ .

Then electric and magnetic field are expressed as the form of plane wave:

$$\overline{E}(\vec{r},t) = \overline{E}(\vec{r})e^{-i\omega t} \tag{2.13}$$
$$\overline{H}(\vec{r},t) = \overline{H}(\vec{r})e^{-i\omega t} \tag{2.14}$$

where $\omega$ denotes the eigen-angular frequency, and $\overline{E}(\vec{r})$ and $\overline{H}(\vec{r})$ are the eigenfunction. These eigenfunction should satisfy the eigenvalue equations :

$$\Theta_E \overline{E}(\vec{r}) \triangleq \frac{1}{\varepsilon(\vec{r})}\nabla \times \{\nabla \times \overline{E}(\vec{r})\} = \frac{\omega^2}{c^2}\overline{E}(\vec{r}) \tag{2.13}$$

$$\Theta_H \overline{H}(\vec{r}) \triangleq \nabla \times \{\frac{1}{\varepsilon(\vec{r})}\nabla \times \overline{H}(\vec{r})\} = \frac{\omega^2}{c^2}\overline{H}(\vec{r}) \tag{2.14}$$

where the two differential operators $\Theta_E$ and $\Theta_H$ are defined by the first equality in each of the above equations.

Because $\varepsilon$ is a periodic function of the spatial coordinate $\vec{r}$, we can apply Bloch's theorem to (2.13) and (2.14) as in the case of the electronic wave equation in ordinary crystals with a periodic potential due to the regular array of atoms. Therefore, $\overline{E}(\vec{r})$ and $\overline{H}(\vec{r})$ are characterized by a wave vector $\vec{k}$ in the first Brillouin zone and a band index n and expressed as :

$$\vec{E}(\vec{r}) = \vec{E}_{\vec{k}n}(\vec{r}) = \vec{u}_{\vec{k}n}(\vec{r})e^{i\vec{k}\cdot\vec{r}} \tag{2.15}$$

$$\vec{H}(\vec{r}) = \vec{H}_{\vec{k}n}(\vec{r}) = \vec{v}_{\vec{k}n}(\vec{r})e^{i\vec{k}\cdot\vec{r}} \tag{2.16}$$

where $\vec{u}_{\vec{k}n}$ and $\vec{v}_{\vec{k}n}$ denote periodic vector functions that satisfy the relations $\vec{u}_{\vec{k}n}(\vec{r}+\vec{a}_i) = \vec{u}_{\vec{k}n}(\vec{r})$ and $\vec{v}_{\vec{k}n}(\vec{r}+\vec{a}_i) = \vec{v}_{\vec{k}n}(\vec{r})$, for i=1, 2, 3.

They can be expanded in Fourier series because of the spatial periodicity of these functions. Then, we can obtain the Fourier expansion as the following form of the eigenfunctions :

$$\vec{E}_{\vec{k}n}(\vec{r}) = \sum_{\vec{G}}\vec{E}_{\vec{k}n}(\vec{G})\exp\{i(\vec{k}+\vec{G})\cdot\vec{r}\} \tag{2.17}$$

$$\vec{H}_{\vec{k}n}(\vec{r}) = \sum_{\vec{G}}\vec{H}_{\vec{k}n}(\vec{G})\exp\{i(\vec{k}+\vec{G})\cdot\vec{r}\} \tag{2.18}$$

Substituting (2.10), (2.17), and (2.18) into (2.13) and (2.14), we obtain the following eigenvalue equations for the expansion coefficients $\{\vec{E}_{\vec{k}n}(\vec{G})\}$ and $\{\vec{H}_{\vec{k}n}(\vec{G})\}$ :

$$-\sum_{\vec{G'}}\kappa(\vec{G}-\vec{G'})(\vec{k}+\vec{G'})\times\{(\vec{k}+\vec{G'})\times\vec{E}_{\vec{k}n}(\vec{G'})\} = \frac{\omega_{\vec{k}n}^2}{c^2}\vec{E}_{\vec{k}n}(\vec{G}) \tag{2.19}$$

$$-\sum_{\vec{G'}}\kappa(\vec{G}-\vec{G'})(\vec{k}+\vec{G})\times\{(\vec{k}+\vec{G'})\times\vec{E}_{\vec{k}n}(\vec{G'})\} = \frac{\omega_{\vec{k}n}^2}{c^2}\vec{H}_{\vec{k}n}(\vec{G}) \tag{2.20}$$

where $\omega_{\vec{k}n}$ denotes the eigen-angular frequency of $\vec{E}_{\vec{k}n}(\vec{r})$ and $\vec{H}_{\vec{k}n}(\vec{r})$. By solving one of these two sets of equations numerically, we can obtain the dispersion relation of the eigenmodes, or the photonic band structure.

This numerical method, which is based on the Fourier expansion of the electromagnetic field and the dielectric function, is so-called the plane wave expansion (PWE) method.
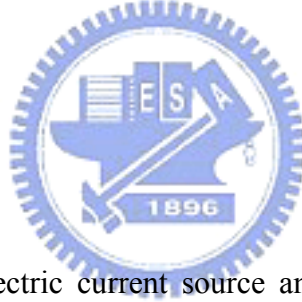
## 2-3.  Finite-Difference Time-Domain Method

To solve the differential form of Maxwell's equations, we can replace the differential form with differencing form, and expand the differencing form to obtain the basic Finite-Difference Time-Domain (FDTD) equation. Because the time-domain technique can cover a wide frequency range with single simulation run, FDTD method is the one of the most popular method to simulate the electromagnetic wave in the photonic crystal.

## 2-3-1.  Maxwell's Equations and Yee Algorithm

As simulating by FDTD method, Maxwell's curl equations are given in the following:

$$\nabla \times \vec{E} = -\frac{\partial \vec{B}}{\partial t} - \overline{J_m}$$
$$\nabla \times \overline{H} = \frac{\partial \overline{D}}{\partial t} + \overline{J_e} \tag{2.21}$$

where $\overline{J_e}$ and $\overline{J_m}$ denote electric current source and magnetic current source. Then, we substitute the relation of them into (2.21). We can obtain:

$$\frac{\partial \vec{E}}{\partial t} = \frac{1}{\varepsilon} \nabla \times \overline{H} - \frac{\sigma}{\varepsilon} \overline{E}$$
$$\frac{\partial \overline{H}}{\partial t} = -\frac{1}{\mu} \nabla \times \vec{E} - \frac{\rho'}{\mu} \overline{H} \tag{2.22}$$

where $\varepsilon$ is the electrical permittivity, $\mu$ is the magnetic permeability, $\sigma$ is the electrical conductivity, and $\rho'$ is an equivalent magnetic resistivity. The magnetic resistivity term is provided to yield symmetric curl equations. By the Maxwell's diverge equation $\nabla \cdot \vec{B} = 0$, $\overline{J_m}$ is absent. Therefore, The magnetic resistivity term is absent. Because of small variation of magnetic permeability in materials, We assume that the magnetic permeability in materials

is equal to that in free space, $\mu_0$. And the material is assumed to be lossless, which implies that $\sigma$ is equal to zero. In a rectangular coordinate system, (2.22) is equal to the following system of scalar equations :

$$\frac{\partial H_x}{\partial t} = \frac{1}{\mu_0}(\frac{\partial E_y}{\partial z} - \frac{\partial E_z}{\partial y}) \tag{2.23}$$

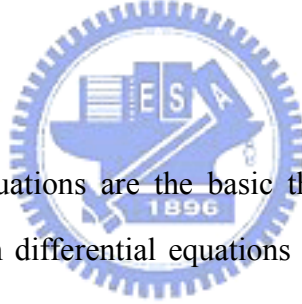$$\frac{\partial H_y}{\partial t} = \frac{1}{\mu_0}(\frac{\partial E_z}{\partial x} - \frac{\partial E_x}{\partial z}) \tag{2.24}$$

$$\frac{\partial H_z}{\partial t} = \frac{1}{\mu_0}(\frac{\partial E_x}{\partial y} - \frac{\partial E_y}{\partial x}) \tag{2.25}$$

$$\frac{\partial E_x}{\partial t} = \frac{1}{\varepsilon}(\frac{\partial H_z}{\partial y} - \frac{\partial H_y}{\partial z}) \tag{2.26}$$

$$\frac{\partial E_y}{\partial t} = \frac{1}{\varepsilon}(\frac{\partial H_x}{\partial z} - \frac{\partial H_z}{\partial x}) \tag{2.27}$$

$$\frac{\partial E_z}{\partial t} = \frac{1}{\varepsilon}(\frac{\partial H_y}{\partial x} - \frac{\partial H_x}{\partial y}) \tag{2.28}$$

The six partial differential equations are the basic the FDTD equations. To do numerical calculation, we shall transform differential equations above into differencing equations. We denote a space point in a rectangular lattice as :

$$(i, j, k) = (i \triangle x, j \triangle y, k \triangle z) \tag{2.29}$$

and for any function of space and time we put :

$$F^n(i, j, k) = F(i \triangle x, j \triangle y, k \triangle z, n \triangle t) \tag{2.30}$$

where $\triangle x$, $\triangle y$, and $\triangle z$ are the lattice space increments in x, y, z coordinate direction, $\triangle t$ is the time increment, and $i, j, k,$ and $n$ are integers. By using the centered finite-difference approximation for the spacial and temporal differential equations, we can obtain :

$$\frac{\partial F^n(i,j,k)}{\partial x} = \frac{F^n(i+\frac{1}{2},j,k)-F^n(i-\frac{1}{2},j,k)}{\triangle x}$$

$$\frac{\partial F^n(i,j,k)}{\partial y} = \frac{F^n(i,j+\frac{1}{2},k)-F^n(i,j-\frac{1}{2},k)}{\triangle y}$$

$$\frac{\partial F^n(i,j,k)}{\partial z} = \frac{F^n(i,j,k+\frac{1}{2})-F^n(i-\frac{1}{2},j,k-\frac{1}{2})}{\triangle x}$$

$$\frac{\partial F^n(i,j,k)}{\partial t} = \frac{F^{n+\frac{1}{2}}(i,j,k)-F^{n-\frac{1}{2}}(i,j,k)}{\triangle t} \tag{2.31}$$

To substitute (2.31) into (2.23 – 2.28), Yee put the components of $\overline{E}$ and $\overline{H}$ at an unit cell of rectangular lattice as shown in Fig. 2-1[10]
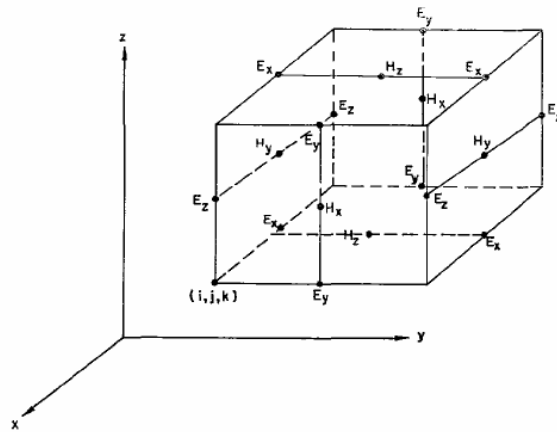


**Fig. 2-1.**   Yee's unit cell. The $\overline{E}$ components are in the middle of the edges and the $\overline{H}$ components are in the center of the faces.[10]

And Yee evaluated $\overline{E}$ and $\overline{H}$ at alternate half time step as shown in Fig. 2-2 :
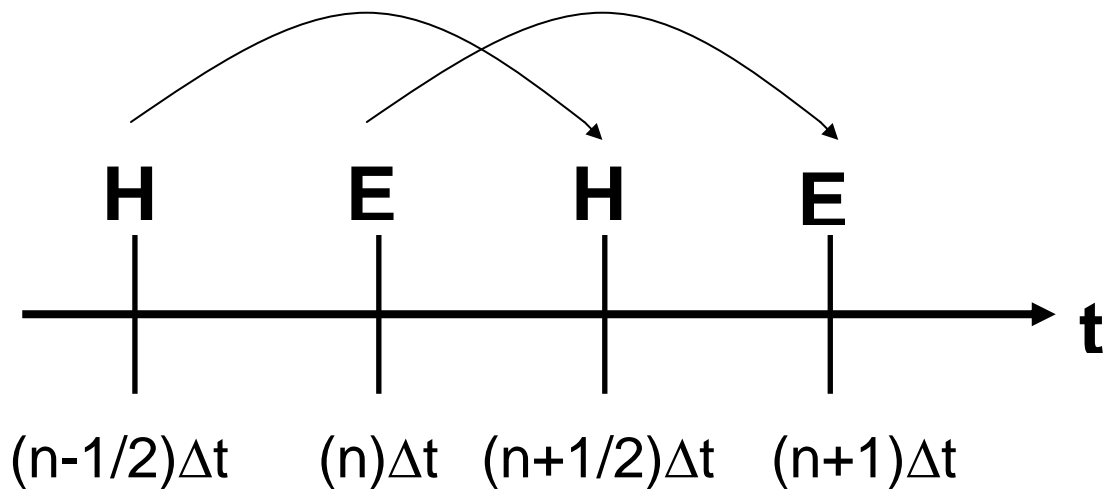


**Fig. 2-2.**   Temporal division of $\overline{E}$ and $\overline{H}$ components.

Then, we substitute (2.31) into (2.25) and (2.28) to obtain $\overline{E}$ and $\overline{H}$ components in the z-direction, we have :

$$H_z^{n+\frac{1}{2}}(i+\tfrac{1}{2},j+\tfrac{1}{2},k) = H_z^{n-\frac{1}{2}}(i+\tfrac{1}{2},j+\tfrac{1}{2},k) + \frac{\Delta t}{\mu_0} \cdot \{\frac{1}{\Delta y}[E_x^n(i+\tfrac{1}{2},j+1,k) - E_x^n(i+\tfrac{1}{2},j,k)]$$

$$- \frac{1}{\Delta x}[E_y^n(i+1,j+\tfrac{1}{2},k) - E_y^n(i,j+\tfrac{1}{2},k)]\} \tag{2.32}$$

$$E_z^{n+1}(i,j,k) = E_z^n(i,j,k+\tfrac{1}{2}) + \frac{\Delta t}{\varepsilon(i,j,k+\tfrac{1}{2})} \cdot \{\frac{1}{\Delta x}[H_y^{n+\frac{1}{2}}(i+\tfrac{1}{2},j,k+\tfrac{1}{2}) - H_y^{n+\frac{1}{2}}(i-\tfrac{1}{2},j,k+\tfrac{1}{2})]$$

$$- \frac{1}{\Delta y}[H_x^{n+\frac{1}{2}}(i,j+\tfrac{1}{2},k+\tfrac{1}{2}) - H_x^{n+\frac{1}{2}}(i,j-\tfrac{1}{2},k+\tfrac{1}{2})]\} \tag{2.33}$$

The equations corresponding to (2.23), (2.24), (2.26), (2.27) can be similarly constructed. By the system of finite-difference equations, the new value of the $\overline{E}$ and $\overline{H}$ component at any lattice point depends only on its previous value and on the previous values of the $\overline{E}$ and $\overline{H}$ component at adjacent points.
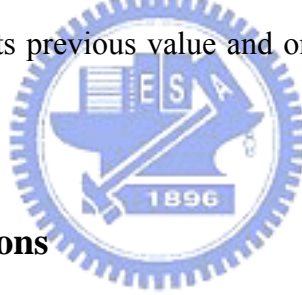
## 2-3-2. Boundary Conditions

There are many electromagnetic calculation for infinite dielectric space, but the practical simulation can calculate infinite dielectric space problem. Therefore, the calculated dielectric space has to be appropriately downscaled. Then, we make an artificial boundary and the electromagnetic field will vanish ta the artificial boundary.

## 2-3-3. Grid Size and Stability Criterion

As the electromagnetic wave propagates in homogeneous dielectric, the propagating velocity in the x, y, z direction is the same. But the propagating velocity in the diagonal direction is faster than that in the x, y, z direction. Therefore, the simulating wave will cause distortion as the propagating time increase. In order to reduce the space error between the x, y,

17

z direction and the diagonal direction, the space grid size must be chosen such that a increment of the electromagnetic field does not change significantly. And the time grid size is also chosen for the stability. For constant $\varepsilon$ and $\mu$, computational stability implies :

$$\Delta t \le \frac{1}{c\sqrt{(\frac{1}{\Delta x})^2 + (\frac{1}{\Delta y})^2 + (\frac{1}{\Delta z})^2}} \qquad (2.34)$$

This requirement puts a restriction on $\Delta t$ for our chosen $\Delta x,\ \Delta y,$ and $\Delta z$.

# Chapter 3. Simulation and Discussion

## 3-1. Introduction

Photonic crystal has attracted lots of attentions due to the possibilities and abilities of controlling the flow of photons in recent years. The electromagnetic wave propagation inside a photonic crystal is forbidden in all directions for a certain frequency range due to photonic band-gap (PBG) effect. The applications of photonic crystal have been widely investigated, such as optical communication systems, quantum optical devices, and optical integrated circuits. Recently, it was suggested to employ radial Bragg layers instead of photonic crystal to confine light in small cavities [11]. The radial structure offers significant advantages for optimal cavity design, primarily because it enable analytic design of the layer structure and optimal tailoring of the cavity size and the reflector periodicity. Unfortunately, the radial Bragg structure is difficult to realize using the suspended membrane concept which was successfully used for photonic crystal cavities. In addition, the upper surface of such structure is not continuous which makes it not suitable for electrical pumping and for realizing electrically pumping lasers. To facilitate that, several analytical and numerical results of circular photonic crystal resonator have been reported [12 - 17], but there are no experimental results for circular photonic crystal cavities. Therefore, we will design smaller circular photonic crystal micro-cavity than these in reports before. And, the existence of photonic band gap and several defect modes of circular photonic crystal cavities can be calculated by using finite-difference time-domain (FDTD) method.

## 3-2. Device Design

The geometry of circular photonic crystal micro-cavity is similar to that of micro-gear laser [18] and the gear has good consistency to the whispering-gallery mode (WGM) at the

cavity edge. The standing wave with azimuthal number equal to half of the gear number will form. Then, the schematic of 2D circular photonic crystal micro-cavity on a dielectric slab is shown in Fig. 3-1 (a). The circular PC patterns formed by air hole with dielectric constant 1.0 are fabricated on a InGaAsP slab with dielectric constant 12.96. The membrane structure is formed by multi-quantum-wells (MQWs) membrane surrounded by air cladding. The lattice geometry of circular PC is also shown in the inset of Fig. 3-1 (b). The numbers of air holes in each concentric ring is proportional to the circumference of each concentric ring. Therefore, the same angular length can be obtained in order to let angular dependence of the perturbation less significant. And, we choose D2 cavity, which means the micro-cavity is formed by removing two-ring air holes (i.e. removing seven air holes from the center of the circular photonic crystal), because the circular photonic crystal has the really circular geometry from third ring and D2 cavity has the smallest micro-cavity size of circular photonic crystal.
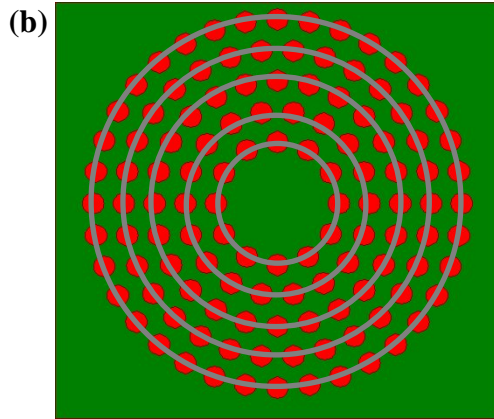


(a)

**(b)**
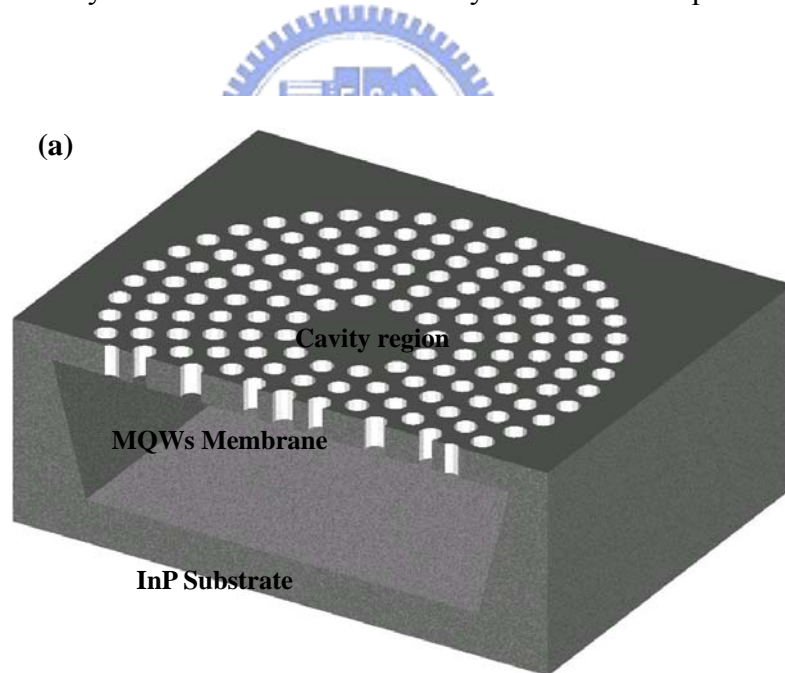


**Fig. 3-1.**  (a) The schematic of a circular photonic crystal micro-cavity laser.

(b) The lattice geometry of circular photonic crystal.

## 3-3.  Symmetry and Photonic Band Gap of Circular Photonic Crystals

In Fig. 3-2, we can find that the circular photonic crystal has the symmetric axes at the angular angle $\pi/6$, and the pattern will rotate $\pi/2$ along each symmetric axes.
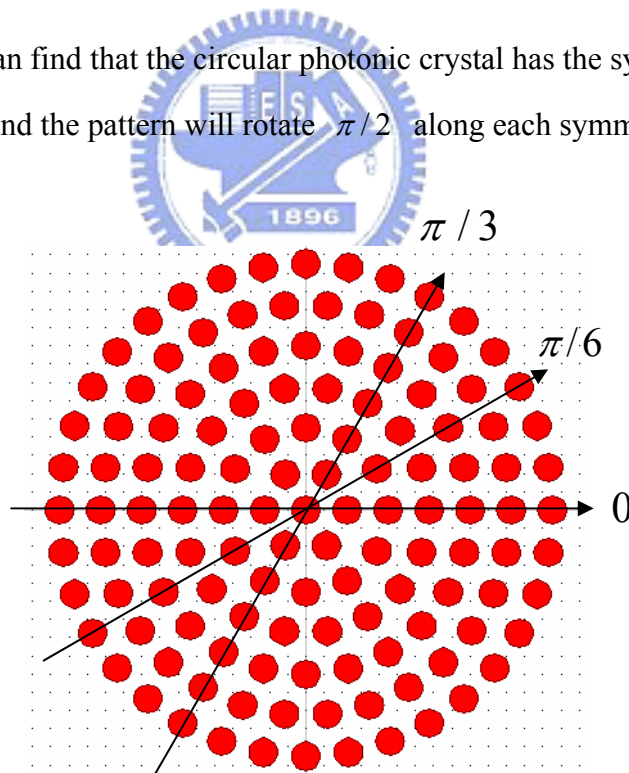


**Fig. 3-2.**  The symmetry of circular photonic crystal.

To explain that there is the photonic band gap in 2D circular photonic crystal, we performed the 2D FDTD analysis with the effective index approximation. We calculated the

transmission spectrum of circular photonic crystal to confirm the photonic band gap. The effective index of the membrane and air holes was assumed to be 2.7 and 1.0. A Gaussian pulse excitation was given for the polarization inside the 2D plane with a central normalized frequency $a/\lambda o$ of 0.3703. Transmission spectrum calculated for r/a=0.35 was shown in Fig. 3-3. The symbol "a" denotes lattice constant, which means the distance of two neighboring air holes and the symbol "r" denotes the radius of air hole.
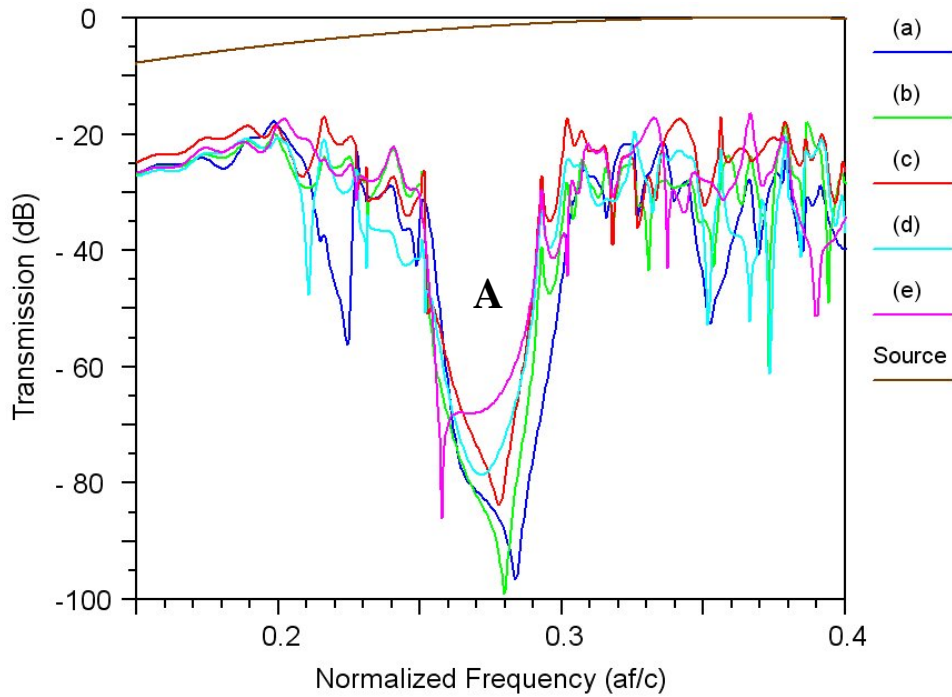


**Fig. 3-3.** Transmission spectrum of circular photonic crystal. The five different incident angles from (a) to (e) is  0, $\pi/18$, $\pi/12$, $\pi/9$, and $\pi/6$.

Against five different incident angles (a) ~ (e), which was chosen by the symmetry, we can find that the transmission is strongly suppressed in frequency range A. In particular, a transmission suppression of ~ 40 dB is observed in frequency range A for five incident angles. Therefore, this range can be though as photonic band gap of this structure. And we can find that the position and width of the photonic band gap are almost independent of the incident angle, hence there is isotropic photonic band gap in the circular photonic crystal.

Because the device is designed for the optical communication, and our MQWs has the photon-luminescence (PL) spectrum centered at 1550nm, we have to optimize the position of the photonic band gap in order to obtain a good alignment between the PL spectrum and the photonic band gap. Therefore, we fix the lattice constant at 520 nm and tune the r/a ratio to change the position of photonic band gap. The transmission spectrum with r/a= 0.38, 0.4, 0.42, and 0.44 is shown in Fig. 3-4.
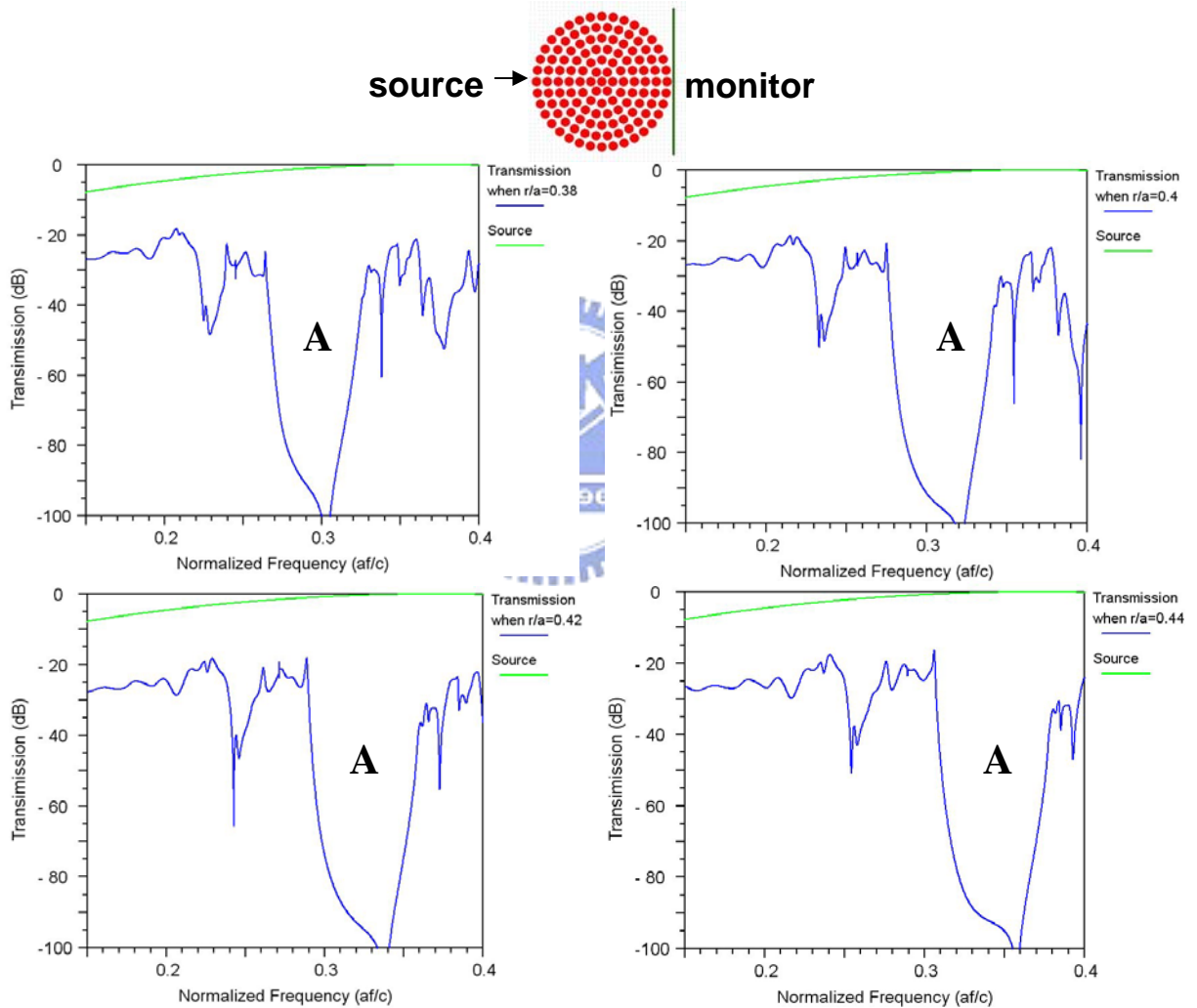


**Fig. 3-4.** The transmission spectrum of circular photonic crystal with r/a= 0.38, 0.4, 0.42, and 0.44 at a fixed lattice constant = 520 nm. The inset shows the simulated structure and the position of the source and the monitor.

By this simulation, we can find that the photonic band gap will still exist and shift to the higher normalized frequency when r/a ratio increases, i.e. the effective index decreases. And the photonic band gap middle lies at the wavelength = 1513 nm and 1591 nm, which is near the PL spectrum peak, when r/a = 0.44 and 0.42. Therefore, we can tune the r/a ratio in the range to obtain the better alignment. And the shift of the photonic band gap versus varying r/a ratio is shown in Fig. 3-5.
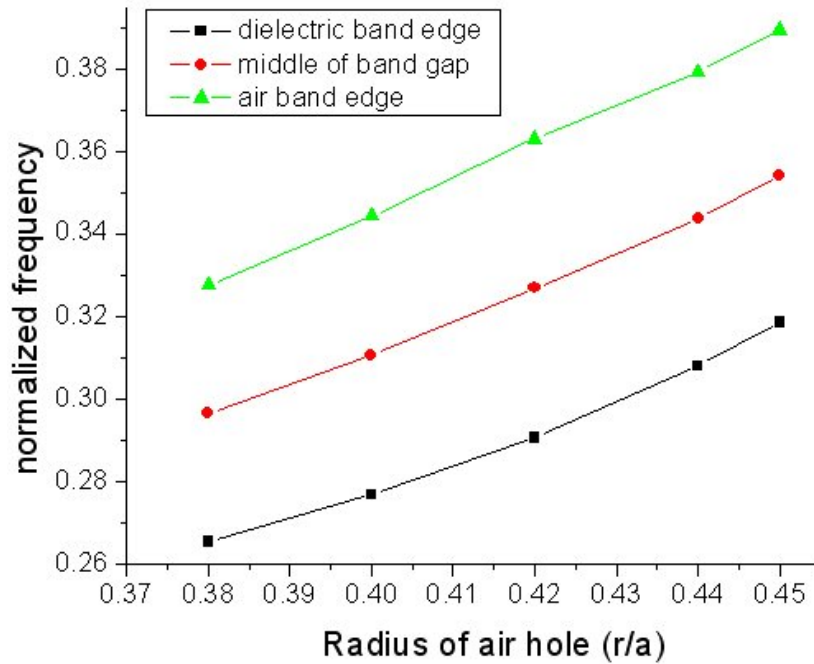


**Fig. 3-5.**   The photonic band gap shifts versus r/a ratio at a fixed lattice constant

By Fig. 3-5, we can find the middle of band gap at the wavelength = 1550 nm when r/a = 0.4297 and fixed lattice constant a = 520 nm.

## 3-4.  Mode Analysis

In order to explain defect modes in 2D circular photonic crystal micro-cavity, we performed the 2D FDTD analysis with the effective index approximation. 2D FDTD simulation is compared with 3D FDTD simulation using circular photonic crystal

micro-cavity, which is form by removing seven air holes. In Fig. 3-6, there is 1% ~ 3% normalized frequency shift in 2D FDTD simulation and no different mode profile is observed. Thus, we confirm the 2D FDTD simulation method is efficient and reliable approach. And, because 3D FDTD simulation is complicated and time-consuming, we use 2D FDTD method to simulate the spectrum and resonant modes below.
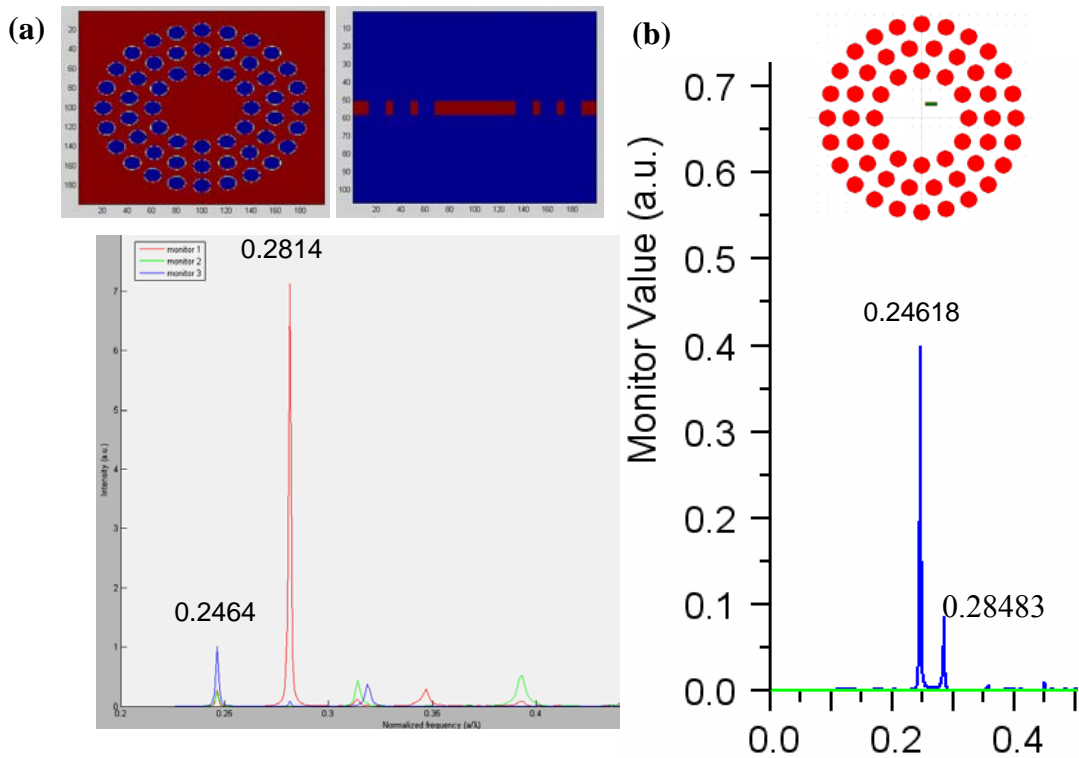


**Fig. 3-6.** (a) The spectrum of D2 circular photonic crystal micro-cavity simulated by 3D FDTD method. The right and the left inset show the structure in the x-y plane and x-z plane.(b) The spectrum of D2 circular photonic crystal micro-cavity simulated by 2D FDTD method. The inset shows the structure in the xy plane.

A D2 circular photonic crystal micro-cavity is simulated by the setup of lattice constant = 526 and the r/a ratio = 0.435. A resonant spectrum is shown in Fig. 3-7. There are eight resonant modes in this spectrum. The two dash line show the photonic band gap. We can find that there are five resonant modes inside the band gap region.
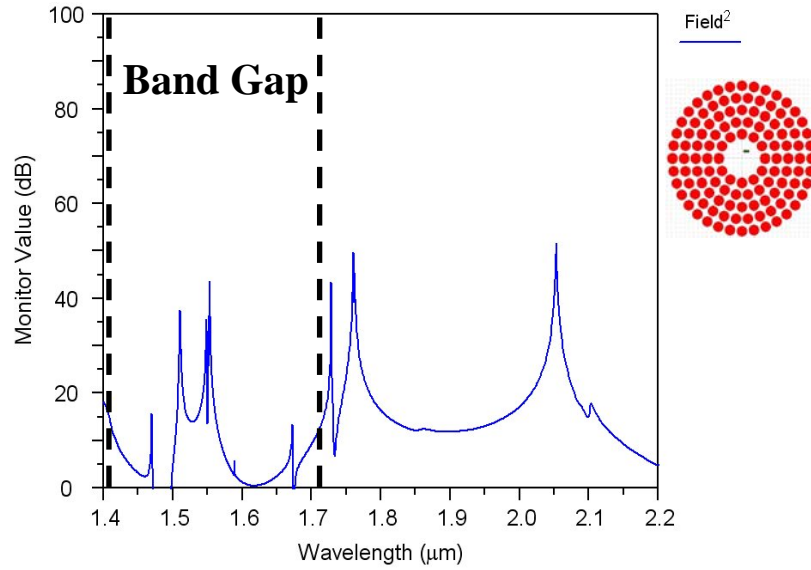
**Fig. 3-7.** The resonant spectrum of D2 circular photonic crystal micro-cavity

In order to analyze the circular photonic crystal micro-cavity, we have to obtain the lasing mode profile by pumping the micro-cavity at each peak wavelength. Then, the normalized frequency $a/\lambda$ of defect modes versus the r/a ratio varied from 0.38 to 0.45 with 520 nm lattice constant was summarized in Fig. 3-8 (a). Here, black plots with solid lines show the numerical results. The gray area indicates the photonic band gap of frequency range **A** in Fig. 3-3. There are eight main defect modes inside photonic band gap. These modes were divided into k=4, k=2, k=0, k=5, WGM (k=6), k=3, k=1, k=6 modes from low to high normalized frequency, where k denotes the rotational Bloch number. The calculated magnetic field distribution of defect modes with 1, 2, 4, 6, 8, 10, 12, and 12 lobes (matches the most inner air holes) corresponding to k=0, k=1, k=2, k=3, k=4, k=6, WGM (k=6) were shown in Fig. 3-8 (b). Here, we proposed to focus on the WGM (k=6), which has standing wave with azimuthal number equal to half of the gear number.
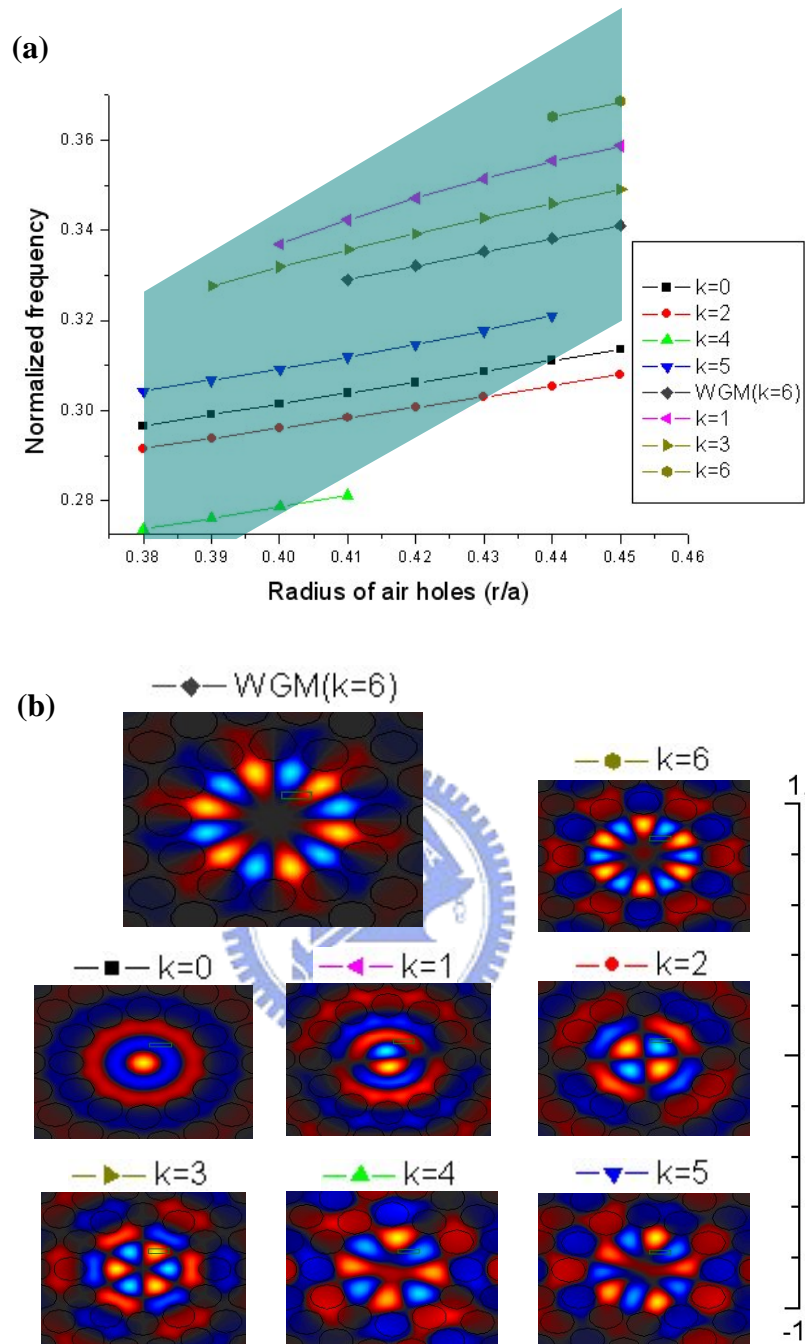
**(a)**



**(b)**



**Fig. 3-8** (a) Calculated resonant mode frequencies of circular PC micro-cavity. Gray area indicates calculated photonic gaps of **A** in Fig. 3-3. (b) The mode profiles correspond to their symbols in Fig. 3-8 (a).

In Fig. 3-8 (a), we can find that the WGM (k=6) separates far away to the other modes, which is a nice characteristic. And the significant node with no field distribution of WGM has potential for the design of current-injected circular photonic crystal micro-cavity. Therefore,

we will focus on the WGM (k=6) in our design so we eliminate these modes with k=4, k=2, k=0, k=5 by letting these modes out of the MQWs gain region, which was discussed in 3-3.

## 3-5.  Side Mode Elimination

An intuitive idea of destroying these modes in the center of cavity and maintaining the WGM is to add central air hole. The central air hole can destroy the electromagnetic distribution in the center of cavity. In order to eliminate some modes in the band gap, we add the central air hole in circular photonic crystal D2 micro-cavity. And, the resonant spectrum is shown in fig. 3-9. The inset shows the mode profiles and the structure with central air hole.
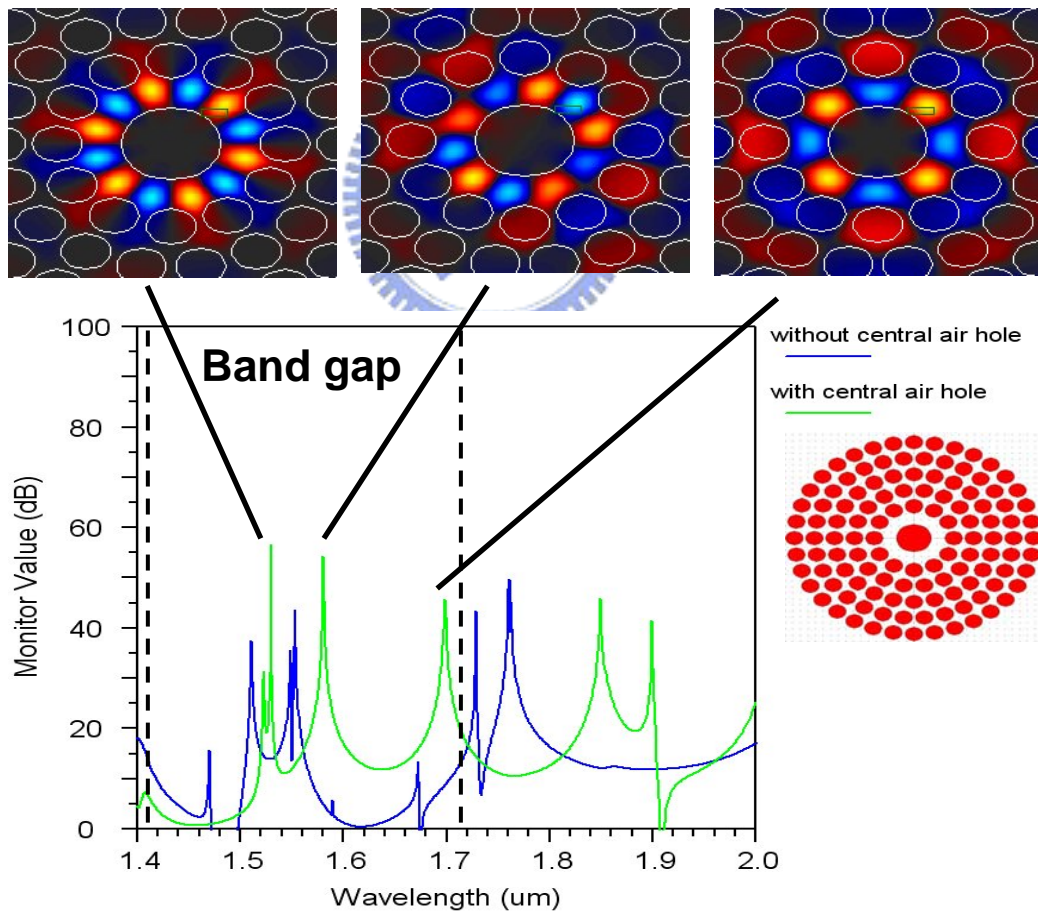


**Fig. 3-9.**  The resonant spectrum of D2 circular photonic crystal micro-cavity with and without central air hole. The inset shows the mode profile and the structure with central air hole.

We can find that the resonant mode peaks was reduced from five to three. And, these eliminated modes are k=1, k=3, k=6 modes. The k=1, k=3 modes are eliminated because its mode profile overlap the central air hole. By adding central air hole, the r/a ratio increases, so the k=6 mode blue shifts to smaller wavelength outside the band gap. After adding central air hole, the three modes inside band gap are all WGM-like modes, which are WGM (k=6), k=5, k=4 form low to high wavelength. From the mode profiles, we can find that WGM (k=6) has good existence and the k=5 and k=4 WGM-like mode profiles were constricted by the central air hole as result of more loss in air holes. Therefore, some resonant modes except WGM (k=6) can be eliminated or reduced by adding central air hole.

# Chapter 4. Fabrication and Measurement

## 4-1. Introduction

The structure design and numerical results for D2 circular photonic crystal micro-cavity have been introduced in chapter 3. In this chapter, the fabrication processes with membrane structure will be introduced. Then the real device of the circular photonic crystal micro-cavity laser with membrane structure will be fabricated and presented. The measurement setup and measured results will be shown and the experiment results will be compared with the numerical results obtained by two-dimensional finite-difference time-domain (FDTD) method.

## 4-2. Fabrication of Photonic Crystal Lasers with Membrane Structure

The epitaxial structure of InGaAsP with compressively strained/unstrained MQWs for membrane structure is shown in Fig. 4-1. The epitaxial structure composed of four 10 nm 0.85% compressively strained InGaAsP quantum wells layers, which are separated by three 20 nm unstrained InGaAsP barrier layers, is treated as active region. The photoluminescence (PL) spectrum of the MQWs with highest gain peak at 1550 nm is shown in Fig. 4-2. The MQWs layers are grown on InP substrate by metalorganic chemical vapor deposition (MOCVD) and then a 60 nm InP cap layer is deposited on the MQWs layers in order to protect the MQWs during a series of dry etching processes.
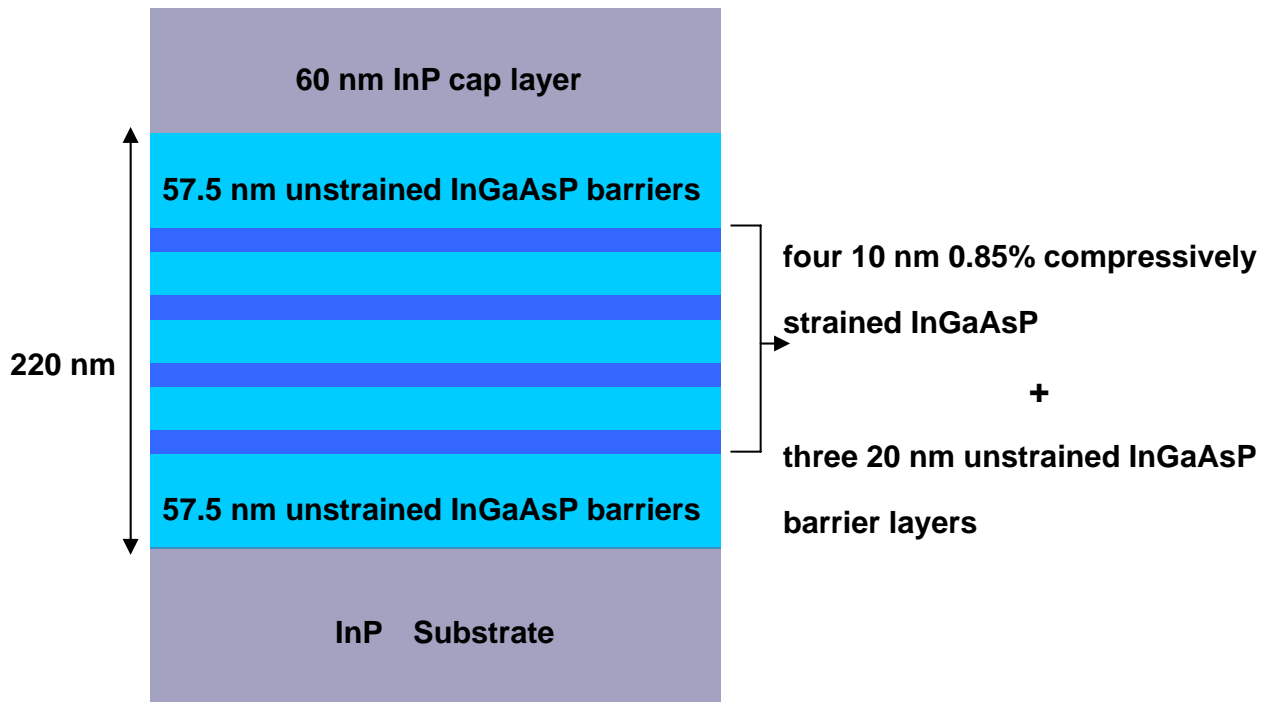
**Fig. 4-1.** The epitaxial structure with compressively strained/unstrained MQWs for photonic crystal lasers with membrane structure. The thickness of the membrane is about 220 nm
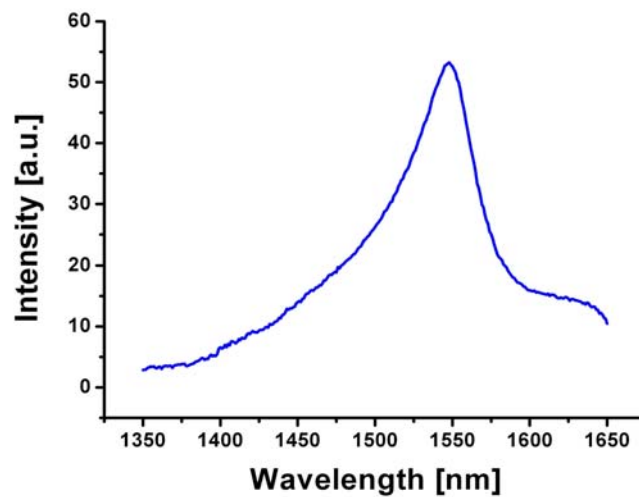


**Fig. 4-2.** The PL spectrum of the MQWs with highest gain peak at 1550 nm

After the epitaxial growth, a hard mask composed of 140 nm $Si_3N_4$ layer is deposited on the sample by plasma enhanced chemical vapor deposition (PECVD). We decide the thickness of $Si_3N_4$ through the selective dry etching ratio in ICP/RIE pattern transfer process. In the fabrication of membrane structure, a 140 nm $Si_3N_4$ hard mask was good enough to let dry etching reaching the depth to 800 nm in InP/InGaAsP layer.

Then, a polymethylmethacrylate (PMMA) resist layer is spun on the sample by a spin coater. Two spinning steps, 1000 rpm for 10 seconds and 4000 rpm for 25 seconds, were used respectively. The photonic crystal pattern is defined by electron-beam lithography (EBL) system. The EBL system is a field-emission scanning electron microscope, which employs a schmasky type fields-emission gun for the electron source and state-of-the-art computer technology for high-resolution image observation.

After the patterns were defined by EBL system, the process of patterns transference will be introduced as follows. The inductively coupled plasma (ICP) and reactive ion etching (RIE) system are used in order to transfer the photonic crystal patterns into InP layer. $Si_3N_4$ hard mask is etched by $CHF_3/O_2$ mixed gas in RIE dry etching process. Before the $Si_3N_4$ hard mask is etched, the sample is etched by $O_2$ plasma in order to clean the residual PMMA around air holes. The $O_2$ plasma is used to remove the PMMA layer after the photonic crystal patterns were transferred into $Si_3N_4$ layer. Then, the photonic crystal patterns are transferred into InP/InGaAsP MQWs layer by $H_2/CH_4/Cl_2$ mixed gas in ICP dry etching process. Afterward, the $Si_3N_4$ hard mask is removed.

In order to fabricate the membrane structure, the InP substrate below the MQWs should be removed. The undercut can be constructed by using a mixture of solution with HCl : $H_2O$ = 4 : 1 at 0℃ for 9 minutes. This process also removes the 60 nm InP cap layer and smoothes the surface and the sidewall of the air holes. This process could be also regarded as a gentle wet etching process to reduce the optical loss caused by the surface roughness. Although wet

etching process is anisotropic, the InP wet etching stops at 95° and 40° from <-1, 0, 0> direction in the (0, -1, -1) plane and the (0, 1, -1) plane because of the InP material characteristic.

The undercut trench under the photonic crystal patterns can be easily formed for the air holes with larger radius. For air holes with smaller radius, the wet etching results in a small wedge-shape undercut in each air hole of photonic crystal. And, the small wedges under each air hole have no chance to meet each other at the corners, so no undercut trench can be formed.

A real device is shown in fig. 4-3. Side view SEM of the circular photonic crystal lasers with membrane structure are shown in fig. 4-3 (a). The V-shaped undercut trench is clearly observed. In fig. 4-3 (b), top view SEM of single circular photonic micro-cavity laser is shown.
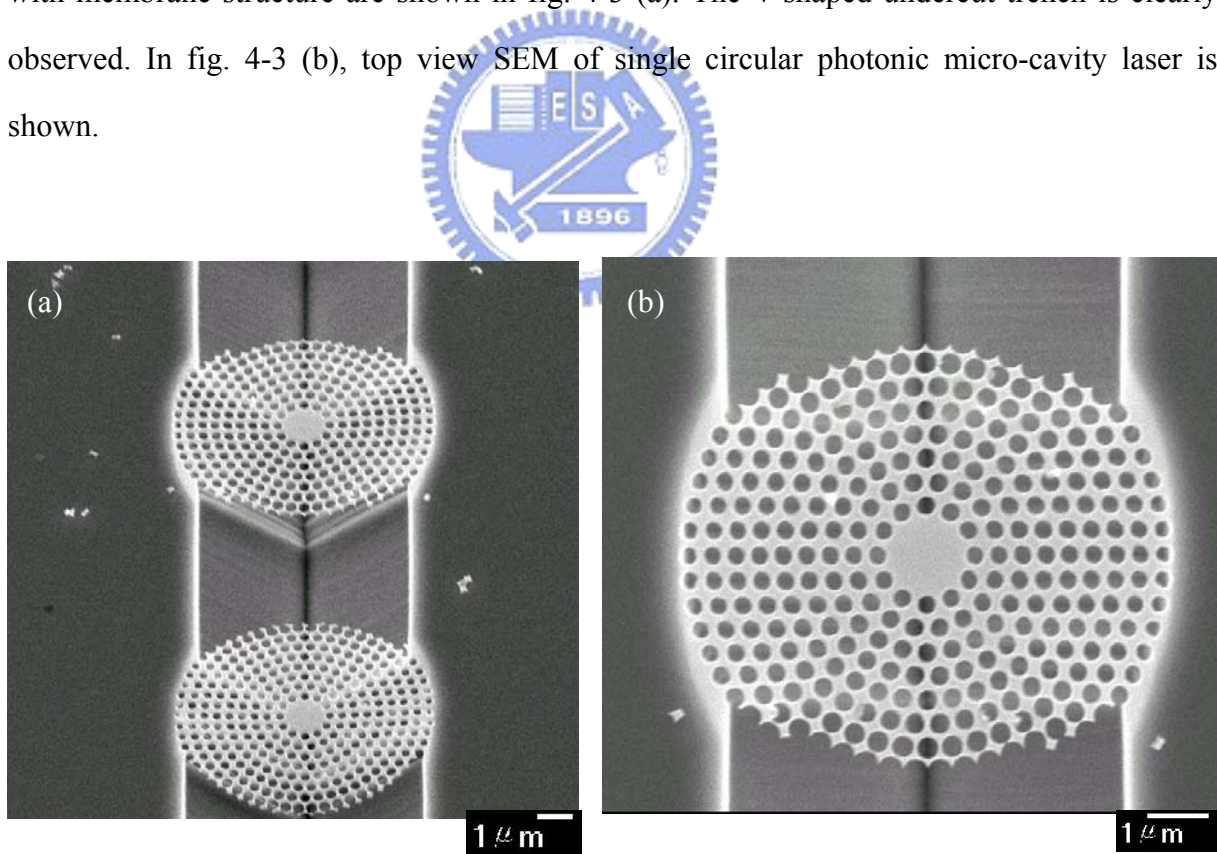


**Fig. 4-3.** **(a)** Side view SEM and **(b)** top view SEM of circular photonic crystal lasers.

An overview of the fabrication processes is shown in Fig. 4-4.
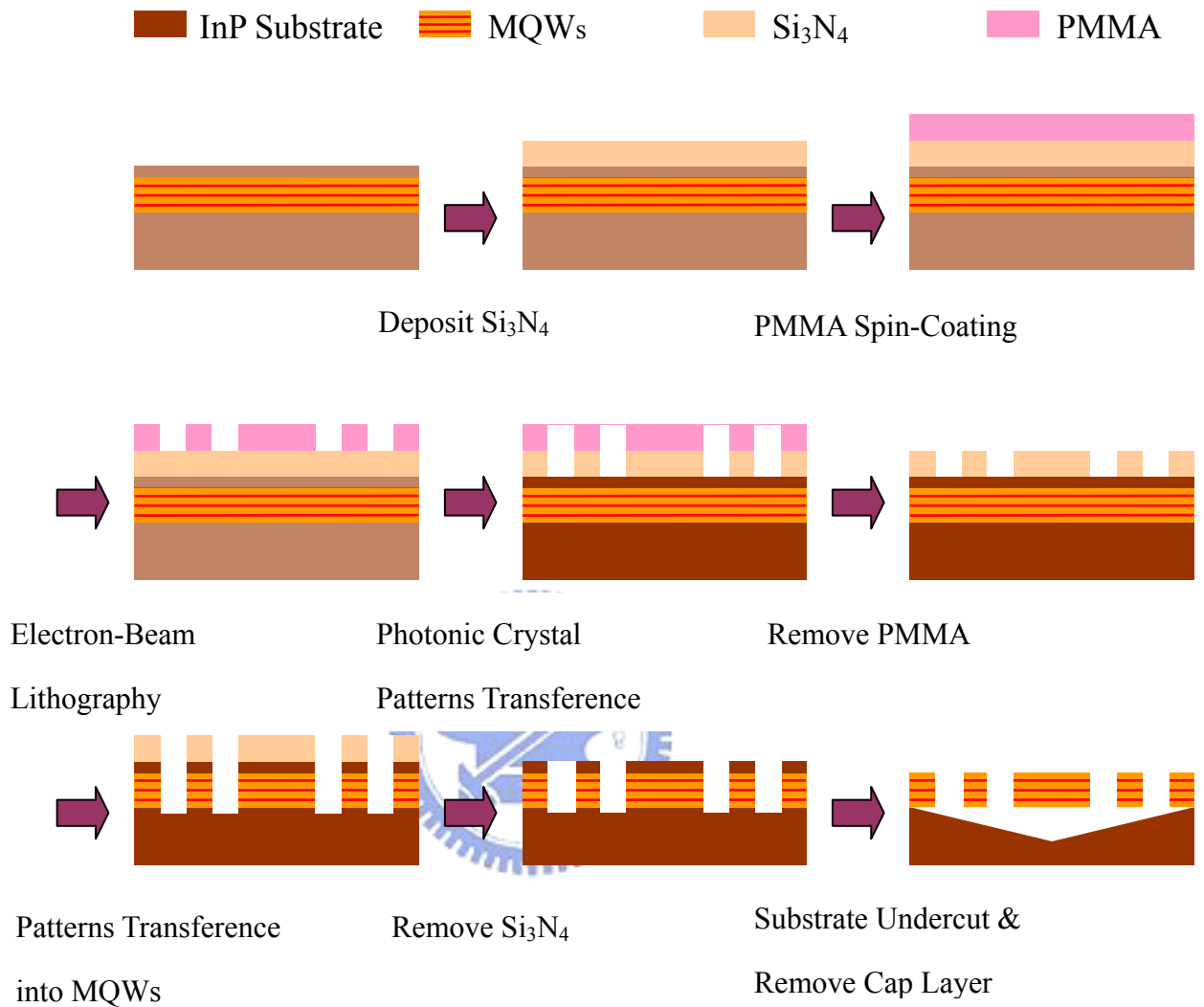


**Fig. 4-4.** The overview of fabrication processes of two-dimensional photonic crystal lasers
with membrane structure.

## 4-3. Circular Photonic Crystal Lasers

The lasing wavelength of the lasers is determined by the lattice constant, the size of
defect, the r/a ratio, and the refraction index of the material, so we can vary lattice parameters
of circular photonic crystal patterns, such as the lattice constant and the r/a ratio in order to
observe the lasing characteristics and obtain the lasing wavelength of two-dimensional

circular photonic crystal laser near the communication wavelength 1550 nm. An array containing 7×12 (rows × columns) circular photonic crystal lasers was fabricated. In a row, the lattice constant increases form 450 nm to 560 nm with the increment 10 nm as the r/a ratio is fixed. In a column, the r/a ratio increases from 0.33 to 0.45 with the increment 0.02 as the lattice constant is fixed. The top view SEM of two-dimensional circular photonic crystal laser array is shown in Fig. 4-5.



100 μm

**Fig. 4-5.** The top view SEM of two-dimensional circular photonic crystal laser array with five different electron dosage.

The top view SEM of single two-dimensional D2 circular photonic crystal laser is shown in Fig. 4-6. The D2 micro-cavity region and the V-shaped under trench can be observed obviously.
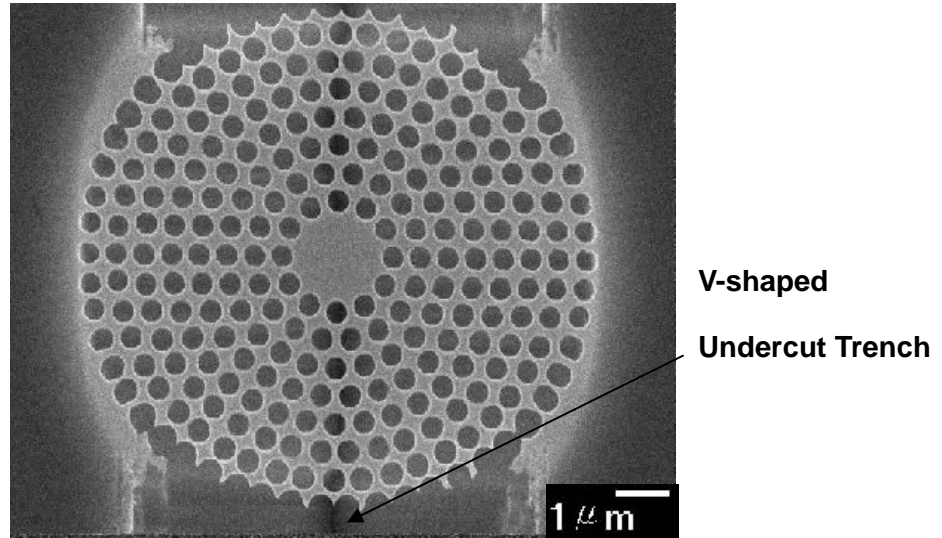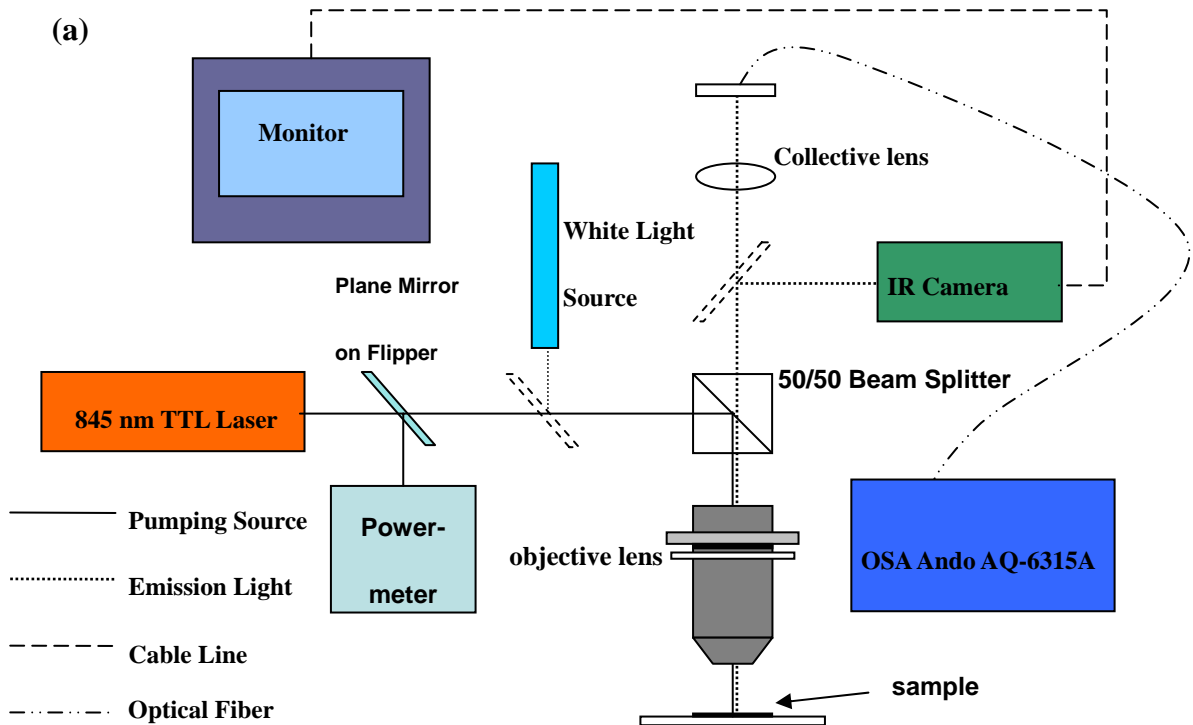
**Fig. 4-6.** The top view SEM of two-dimensional D2 circular photonic crystal laser.

## 4-4. Measurement Results and Analysis

## 4-4-1. Measurement Setup

In order to obtain the characteristics of the fabricated circular photonic crystal micro-cavity laser, we record pulsed room-temperature photoluminescence (PL) spectrum of the laser by using a micro-PL system with sub-micro-scale special resolution and sub-nanometer-scale resolution in spectrum. The simple setup is shown in Fig 4-7 (a) and the photo is shown in Fig 4-7 (b).
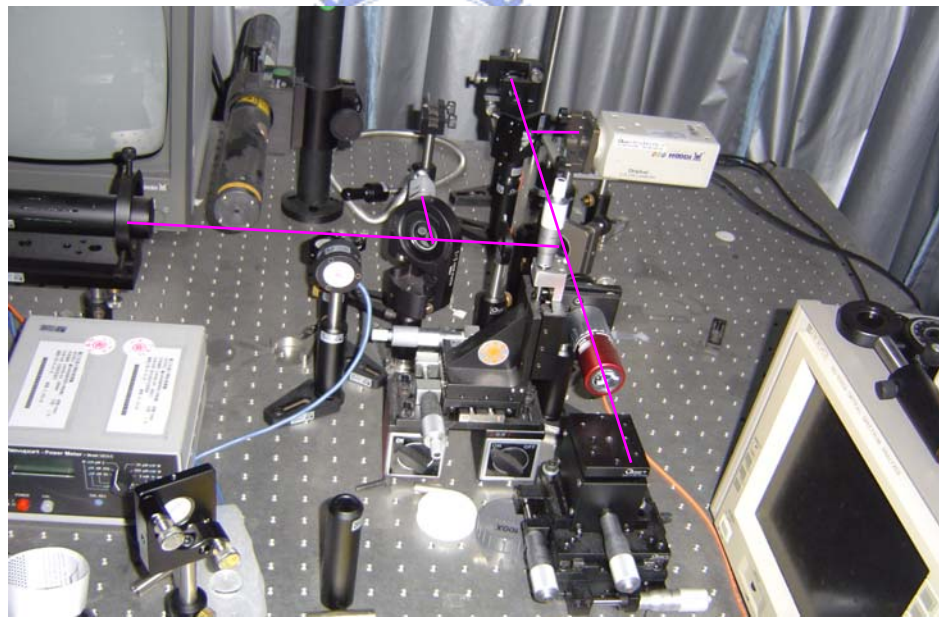
**Fig. 4-7.** **(a)** The setup of micro-PL system. **(b)** The photo of real micro-PL system.

In this system, an 845 nm TTL laser with focused pump spot size about 1.5um is used as the pump source. This TTL laser can be used in pulse operation and continuous-wave operation by switching a function generator. The pulse width of the pump beam is 25 ns with 200 KHz repetition rate. The pump beam is reflected into a 50x long working distance NIR

objective lens which is mounted on a 3-axis stage with numerical aperture of 0.5 by a 50/50 beam splitter, which has 48% reflection in angle 45° of the splitter for 845 nm wavelength is confirmed. The output light from the top of the sample is collected by the objective lens and we use a collective lens to focus the output signal into the slit of our optical spectrum analyzer (OSA) with 0.05 nm resolution. And, the plane mirror can be flipped in order to reflect the pump source into the power-meter when the threshold is measured. All the measurement results were measured by the micro-PL system.

### 4-4-2.    Modes Identification

First, we measured the resonant spectrum of fabricated device to identify these resonant modes. The constitutive resonant spectrum in dB scale is shown in Fig. 4-8. Each resonant mode can be addressed through comparing with numerical results. The measured peaks with normalized frequencies $a/\lambda$ 0.34175, 0.34787, 0.35395, 0.36235 from low to high frequency correspond to WGM (k=6), k=3, k=1, k=6 modes with normalized frequencies $a/\lambda$ 0.33975, 0.34772, 0.35747, 0.36743 in numerical results. The slight shift of frequency is owing to the 2D approximation simulation, which is discussed before.
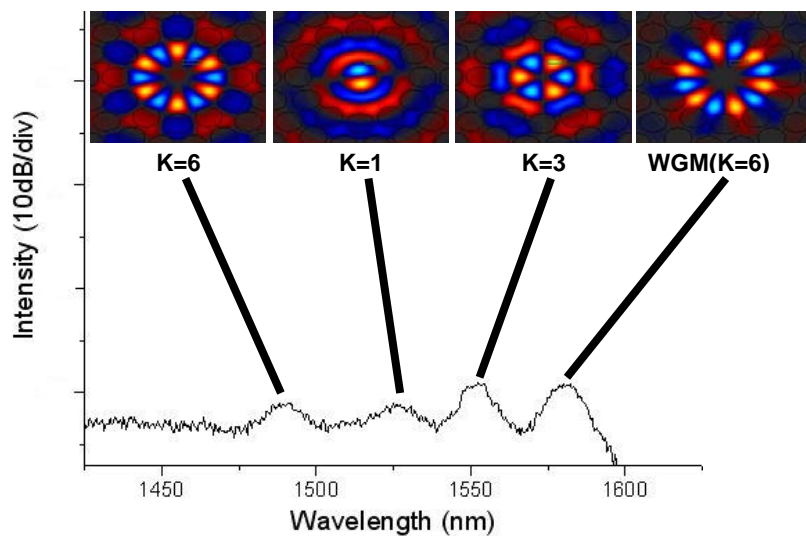


**Fig. 4-8.**    Measured resonant spectrum with 200 nm span and the calculated magnetic field distribution of each resonant mode.

Then, we increase the pump power in order to obtain the lasing spectrum. The lasing spectrum is shown in Fig. 4-9. By comparing the lasing spectrum to the resonant spectrum in Fig. 4-8, we can identify that the lasing mode is the WGM (k=6) and the side mode is the dipole (k=1) mode. Therefore, we confirm that the lasing mode is WGM (k=6). The WGM conform to what we want, which was discussed in 3-4.
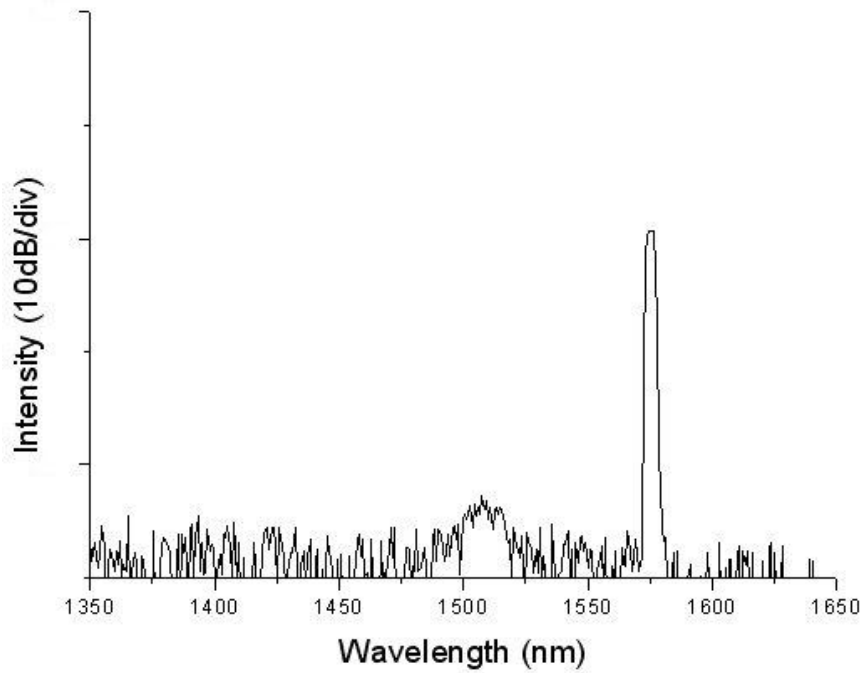


**Fig. 4-9.** The lasing spectrum in dB scale.

## 4-4-3. Lasing Characteristics

A plot of the output power versus input pump power for a typical 2D photonic crystal circular micro-cavity laser is shown in Fig. 4-10. As the input pump power increased, the lasing of the WGM (k=6) was excited. Its threshold is as low as 0.13 mW. As the input pump power is larger than 5.5 mW, the rolling-off effect is observed. This effect is accused for the small cavity size about 1.5 um in diameter and the poor heat dissipation in the surrounding air. The lasing spectrum above threshold is shown in Fig. 4-11. The lasing wavelength is 1574.35 nm and the measured full width at half maximum (FWHM) is 0.13 nm, which is limited by

our optical spectrum analyzer. The inset in Fig. 4-11 show the lasing spectrum below

threshold with 2 nm span and the FWHM is 0.15 nm. The mode peak above the threshold is

25 dB higher than the background spontaneous emission level. On the other hand, the single

mode lasing is observed. The quality factor about 10000 is estimated from the measured
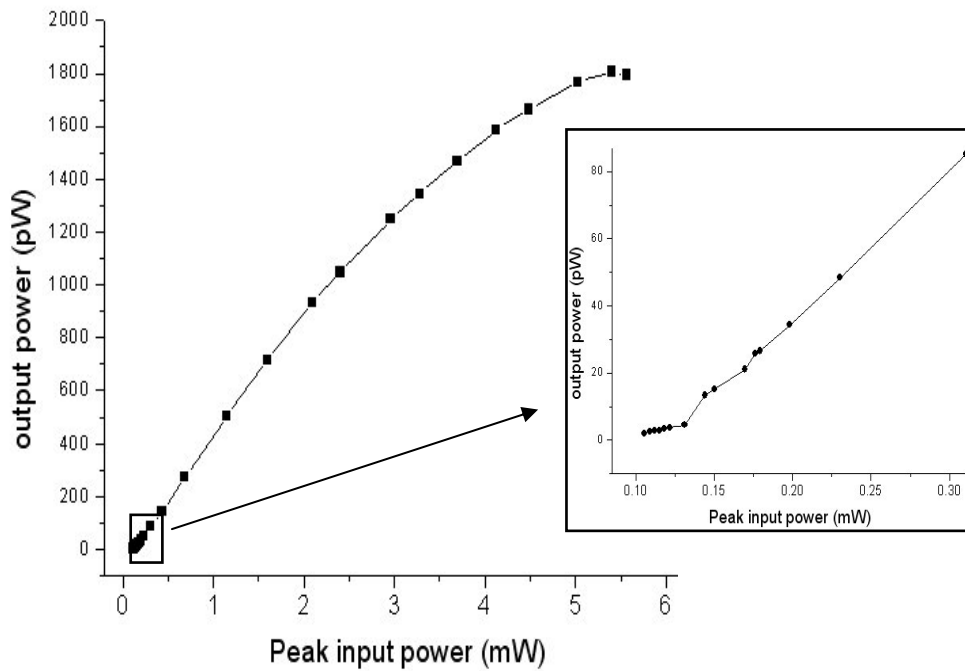
line-width below the threshold pump power.



**Fig. 4-10.** L-L curve of the WGM (k=6). The threshold of ~0.13 mW was observed in the

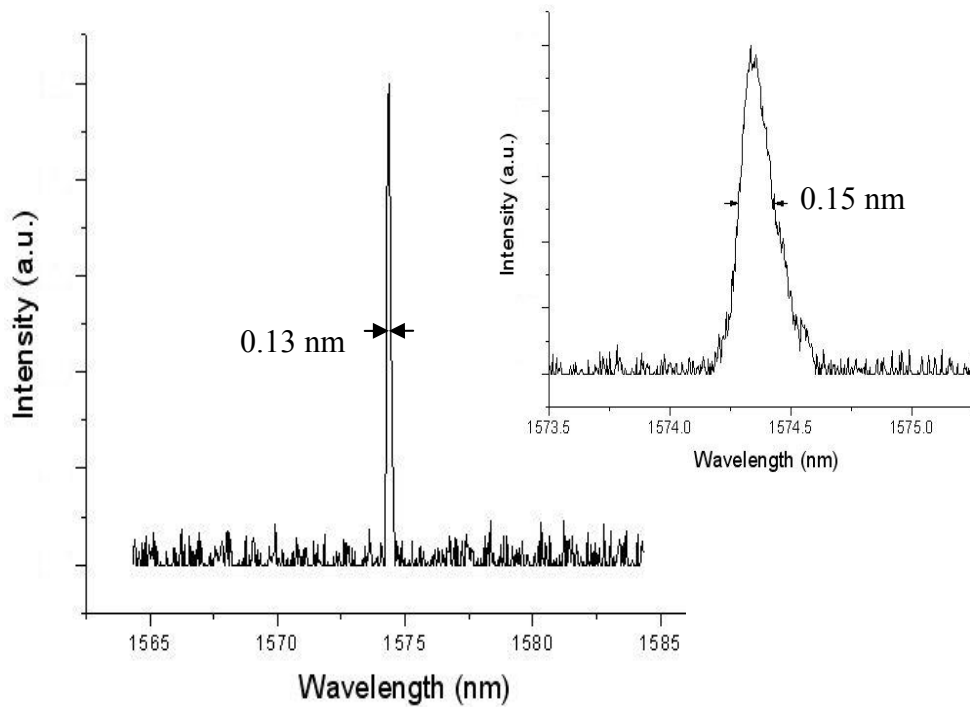inset and the rolling-off effect occurred as the input pump power was larger than

5.5 mW.

**Fig. 4-11.**   Lasing spectrum above threshold of the WGM (k=6). The lasing wavelength is 1574.35 nm. The inset shows lasing spectrum below threshold with 2 nm span.

In addition, single mode lasing is observed from 1456.8 nm to 1594.8 nm without any mode hopping when we measured a row lasers, which vary lattice constant from 490 nm to 550 nm with a fixed r/a ratio as shown in Fig. 4-12. The intensity of each lasing wavelength is normalized.
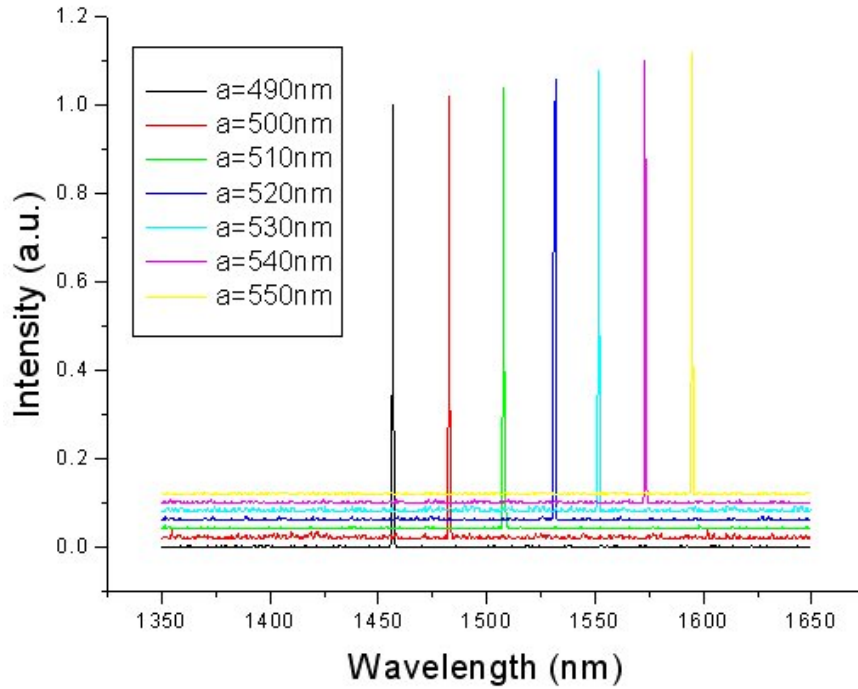
41

**Fig. 4-12.** The lasing wavelengths of a row lasers with varied lattice constant form 490 nm to 550 nm and a fixed r/a ratio.

We can find that the wavelength interval between lasing peaks is almost equal. The interval has the maximum of 26 nm and the minimum of 20 nm. The little difference is caused by small differences of the r/a ratio due to fabrication variation. This large tuning range results from the lasing mode far away to the other modes. The large-range single-mode lasing has advantage of the tolerance of design and fabrication.

## 4-4-4. Comparison between Measurement and Numerical Results

By measuring the array lasers, many measurement results of 2D circular photonic crystal micro-cavity lasers can be obtained. Therefore, we will compare the measurement results to the numerical results as follows. The normalized frequency $a/\lambda$ of defect modes versus the r/a ratio varied from 0.38 to 0.45 with 520 nm lattice constant was summarized in Fig. 4-13. Here, white circles and black plots with solid lines show the measurement results and numerical results. The gray area indicates the photonic band gap of frequency range A in Fig.

3-3. There are eight main defect modes inside photonic band gap. These modes were divided into k=4, k=2, k=0, k=5, WGM (k=6), k=3, k=1, k=6 modes from low to high normalized frequency, where k denotes the rotational Bloch number. Here, we proposed to focus on the WGM (k=6), which has standing wave with azimuthal number equal to half of the gear number. In our design, these modes with k=4, k=2, k=0, k=5 was eliminated by letting these modes out of the MQWs gain region. The calculated magnetic field distribution of defect modes with 12 lobes corresponding to WGM (k=6) is shown in the inset. The WGM separates far away to the other modes, which is a nice characteristic and the significant node with no field distribution of WGM has potential for the design of current-injected circular photonic crystal micro-cavity laser.
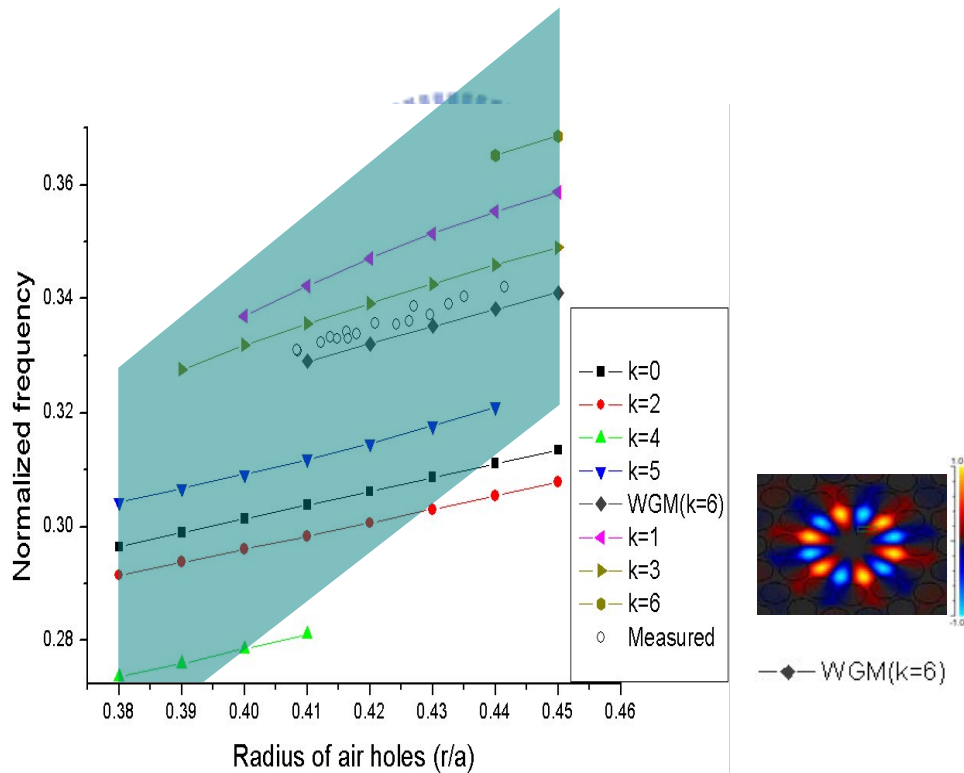


**Fig. 4-13.** Calculated resonant mode frequencies of circular photonic crystal micro-cavity. The white circles denote the measured lasing frequencies. Gray area indicates calculated photonic band gaps of A in Fig. 3-3. The inset shows the calculated magnetic field distribution of WGM (k=6).

## 4-4-5. Side Mode Reduction

Because the side mode is k=1 mode, we add a central air hole in circular photonic crystal in order to eliminate k=1 mode. And, the size of central air hole was chosen for no effect on the lasing WGM (k=6). We measured the lasing spectrum in dB scale with and without central air hole as shown in Fig. 4-14. The modified circular photonic crystal laser with central air hole was fabricated and top view SEM is shown inset. And the reduced side mode profile is also shown inset.
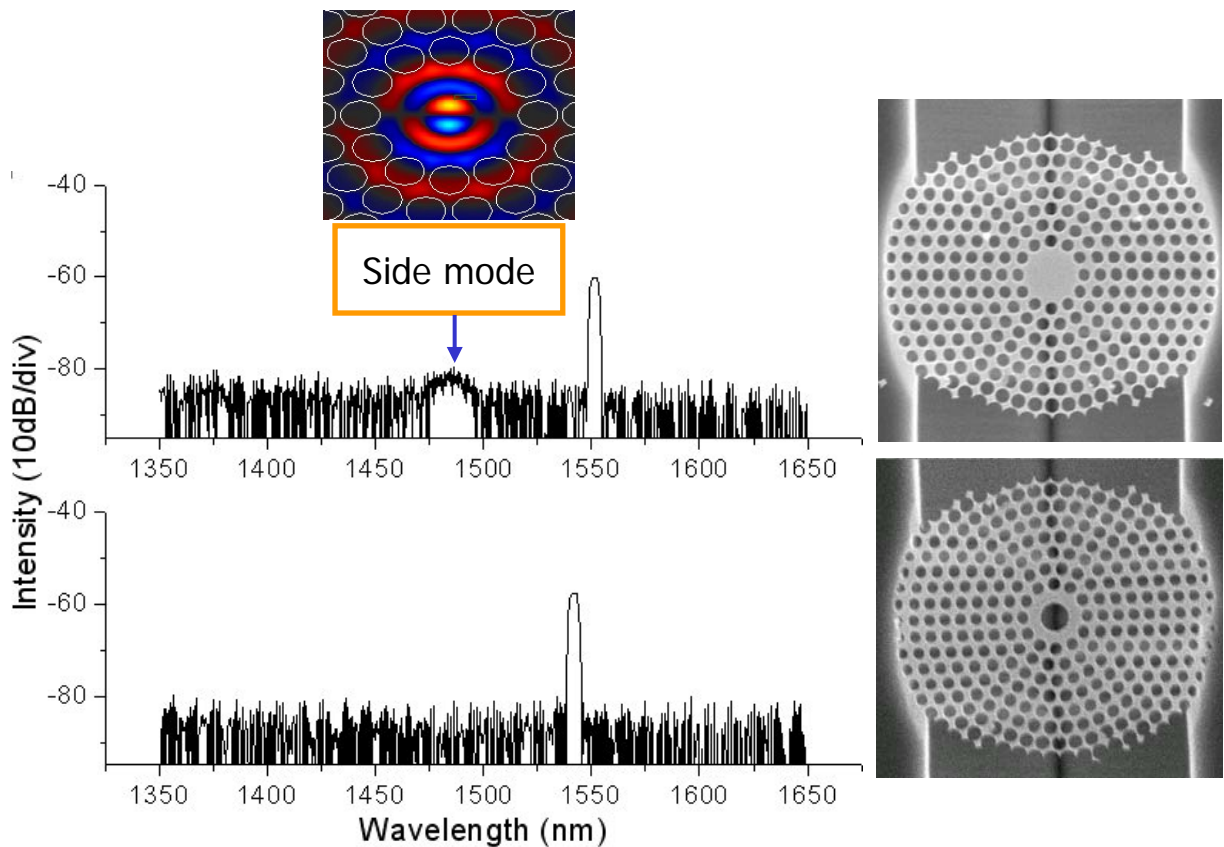


**Fig. 4-14.**   The lasing spectrum of circular photonic crystal with and without central air hole. The top view SEM of real device and the side mode profile are shown inset. The side mode is effectively reduced by adding central air hole.

In Fig. 4-14, we can find that the side mode is effectively reduced and the SMSR increase 5 dB after adding the central air hole. Because the lasing mode was not affected by the central air hole, we can newly identify that the lasing mode is WGM.

Then, we measured the L-L curve of D2 circular photonic crystal micro-cavity laser with and without central air hole as shown in fig. 4-15. In order to diminish the effect of QW gain-region, we choose approximate lasing wavelength.
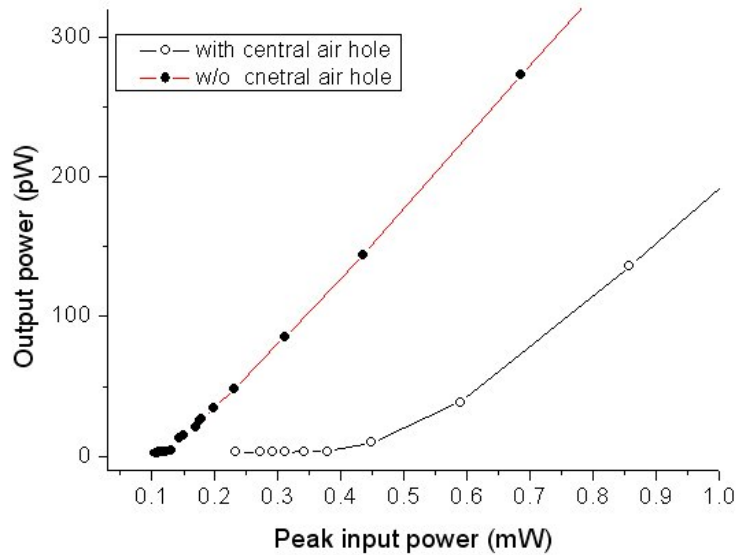


**Fig. 4-15.** L-L curve of D2 circular photonic crystal micro-cavity laser with and without central air hole.

We can find that the threshold of D2 circular photonic crystal micro-cavity laser with and without central air hole is 0.445 mW and 0.131 mW. The higher threshold of laser with central air hole is because the destroyed cavity region resulted in less photon distributing at cavity region.

## 4-4-6. Lasing Characteristics Comparison between Circular Photonic Crystal and 12 Fold Quasi-Photonic Crystal Lasers

The 12 fold quasi photonic crystal D2 micro-cavity has several characteristics like circular photonic crystal D2 micro-cavity, such as the 12 most inner air hole around the cavity ,the WGM (k=6) lasing action, and the cavity size [19]. Therefore, we compare the circular photonic crystal lasers with 12 fold quasi photonic crystal lasers. The top view SEM of circular photonic crystal and 12 fold quasi photonic crystal lasers are shown in Fig. 4-16.
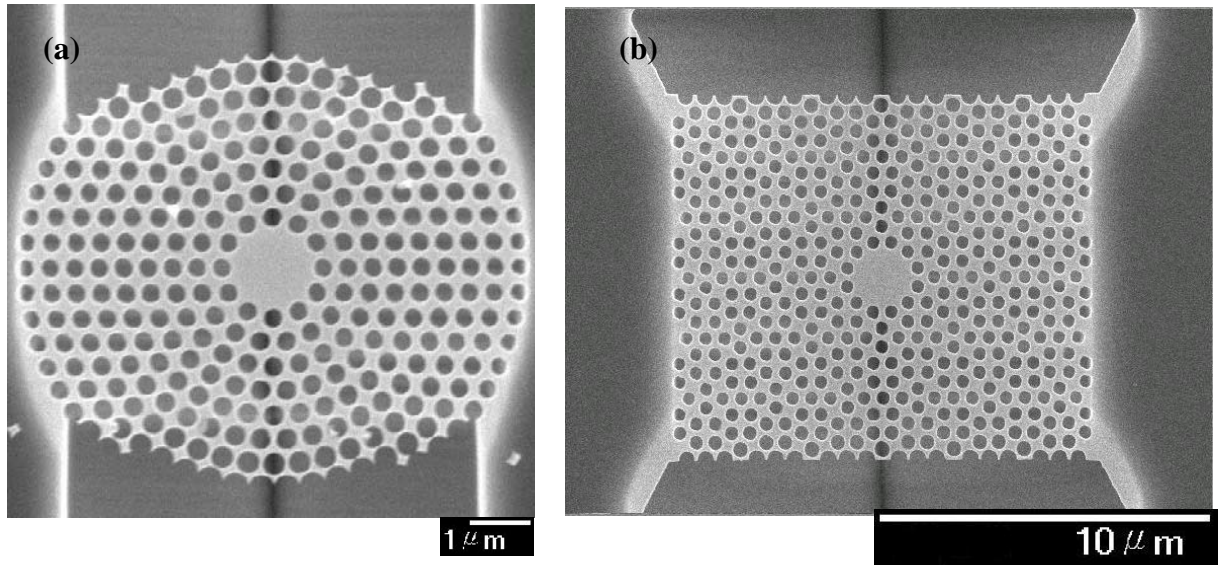
**Fig. 4-16.** Top view SEM of (a) circular photonic crystal laser and (b) 12 fold quasi photonic crystal laser

To reduce the domination of MQWs gain region, we choose the near lasing wavelength of the two lasers. The lasing spectrum of circular photonic crystal and 12 fold quasi photonic crystal are shown in Fig. 4-17. The lasing wavelength is 1574.35 nm and 1571.66 nm, respectively. And, the FWHM is 0.15 nm and 0.37 nm, respectively. We can find that the FWHM of circular photonic crystal laser is thinner than that of 12 fold quasi photonic crystal. Therefore, the quality factor of circular photonic crystal laser is higher than Q of 12 fold quasi photonic crystal. It means that the circular photonic crystal has better confinement for the WGM (k=6). That is because the circular photonic crystal micro-cavity confirm to the micro-disk theory.
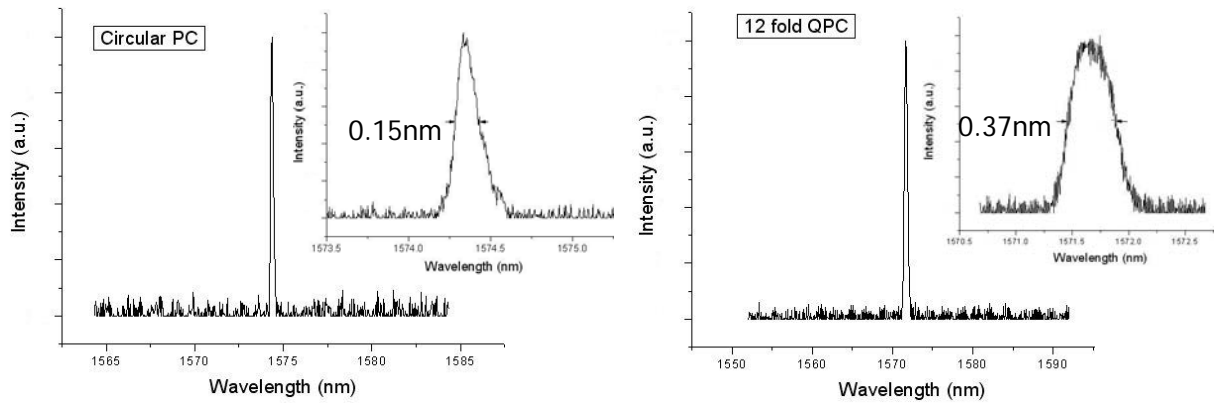
**Fig. 4-17.** Lasing spectrum above threshold of the WGM (k=6). The lasing wavelength is 1574.35 nm and 1571.66, respectively. The inset shows lasing spectrum below threshold with 2 nm span.

The L-L curve of circular photonic crystal and 12 fold quasi photonic crystal lasers is shown in Fig. 4-18. The threshold of circular and quasi photonic crystal laser is 0.131 mW and 0.208 mW, respectively. The lower threshold of circular photonic crystal laser is because the efficient photonic band gap confinement and the total internal reflection confinement of the large r/a ratio are provided by circular photonic crystal. The rolling-off effect is observed at 5.5 mW and 3.3 mW, respectively. From this, we can find that the circular photonic crystal laser has weaker thermal effect than the 12 fold quasi photonic crystal. This is because circular photonic crystal laser has smaller device size. From discussion above, we can find that the circular photonic crystal laser has better lasing characteristics 12 fold quasi photonic crystal laser.
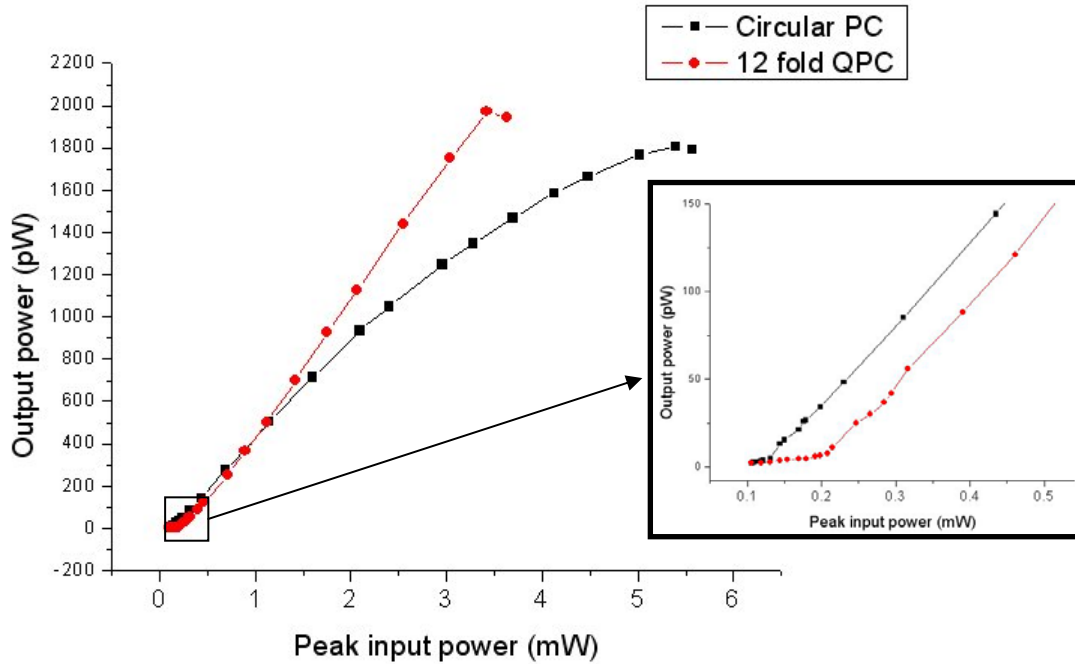
**Fig. 4-18.** L-L curve of the circular and 12 fold quasi photonic crystal laser. The thresholds are estimated to be 0.131 and 0.208 mW, respectively. The rolling-off effect is observed at 5.5 mW and 3.3 mW, respectively

## 4-5. Summary

In this chapter, the fabrication processes of photonic crystal micro-cavity lasers were introduced. The photonic crystal patterns are defined by EBL and a series of dry etching process. The membrane structure is formed by HCl selective wet etching. Then, the real 2D circular photonic crystal micro-cavity lasers were fabricated.

We set up a micro-PL system with nano-scale spectrum resolution to measure the devices. The lasing mode and these resonant modes were identified by comparing the measurement results with the numerical results, so we can identify that the lasing mode and the side mode are WGM (k=6) and k=1 mode, respectively. The basic characteristics including the L-L curve, the lasing spectrum were measured. By measuring the array lasers, we can obtain the illustration of normalized frequency a/$\lambda$ versus the r/a ratio and compare with numerical

results to check the lasing mode, again. By tuning lattice constant, We obtained a large single-mode lasing range of 140 nm without any mode hopping. And, The side mode was reduced by adding central air hole. Finally, we compared the lasing characteristics between the circular and 12 fold quasi photonic crystal laser.

# Chapter 5. Conclusion

In this thesis, the history and the basic theory of the photonic crystal were introduced. Then, the application and the evolution of photonic crystal micro-cavity lasers were also introduced.

The theory and the methodology of simulation including plane-wave-expansion (PWE) and finite-difference time-domain (FDTD) were presented. The structure design was simulated. We defined that there is the photonic band gap in the circular photonic crystal by using transmission spectrum. And, we explained that the defect modes is confined by the photonic band gap and gained the magnetic field distribution of these modes. Some modes can be eliminated by adding central air hole.

In the fabrication, we presented the fabrication processes of two-dimensional photonic crystal micro-cavity lasers with membrane structure. Then, an array containing $7 \times 12$ (rows $\times$ columns) circular photonic crystal lasers was fabricated. In order to characterize the circular photonic crystal lasers, a micro-scale photoluminescence (PL) system with sub-micro-scale special resolution and sub-nanometer-scale resolution in spectrum was set up and used for measurement. By using the PL system, the lasing and resonant spectrum were obtained. Then, we identified the lasing mode and resonant modes by comparing the measurement results with numerical results. The basic characteristics of two-dimensional circular photonic crystal micro-cavity lasers including the L-L curve, the lasing spectrum were presented. We reduced the side mode by adding central air hole. And, we obtained the circular photonic crystal has good confinement for WGM by compare the lasing characteristics with 12 fold quasi photonic crystal laser.

# References

[1]   E. Yablonovitch,” Inhibited spontaneous emission in solid-state physics and electronics” *Phys. Rev. Lett*. **vol. 58,** pp. 2059-2062, (1987)

[2]   J. D. Joannopoulos, R. D. Meade, J. N. Winn, *Princeton University Press*, (1995)

[3]   P. R. Berman, *New York:Academic*, (1994)

[4]   O. Painter, R. K. Lee, A. Scherer, A. Yariv, J. O. O’brien, P. D. Dapkus, and I. Kim,” Two-dimensional photonic band-gap defect mode laser ” *Science* **vol. 284,** pp. 1819-1821, (1999)

[5]   O. Painter and K. Srinivasan,” Polarization properties of dipolelike defect modes in photonic crystal nanocavities “ *Opt. Lett.* **vol. 27**, 339-341, (2002)

[6]   W. Kuang, J. R. Cao, S. J. Choi, J. D. O’Brien and P. D. Dapkus,” Modified suspended membrane photonic crystal D3 laser cavity with improved sidemode suppression ratio” *IEEE Phton. Technol. Lett*. **vol. 17**,941-943, (2005)

[7]   H. G. Park, S. H. Kim, S. H. Kwon, Y. G. Ju, J. K. Yang, J. H. Baek, S. B. Kim, and Y. H. Lee,” Electrically driven single cell photonic crystal laser ” *Science* **vol. 305,** 1444-1447. (2004)

[8]   M. Imada, S. Noda, A. Chutinan, T. Tokuda, M. Murata, and G. Sasaki,” Coherent two-dimensional lasing action in surface-emitting laser with triangular-lattice photonic crystal structure” *Phys. Lett.* **vol. 75,** 316-318. (1999)

[9]   K. Srinivansan, P. E. Barclay, and O. Painter,” Experimental demonstration of a high quality factor photonic crystal microcavity” *Appl. Phys. Lett.* **vol.83,** 1915-1917. (2003)

[10]   K. S. Yee, *IEEE Trans. Antennas Propag*., “Numerical solution of initial boundary value problems involving Maxwell’s equations in isotropic media” **vol. 14,** pp. 302-307, (1966)

[11]   J. Scheuer, W. M. Green, G. DeRose and A. Yariv,” Lasing from a circular Bragg nanocavity with an ultrasmall modal volume” *Appl. Phys Lett*. 86 , 251101 (2005).

[12]   J. Scheuer and A. Yariv, " Coupled-Waves Approach to the Design and Analysis of Bragg and Photonic Crystal Annular Resonators" *IEEE J. Quantum Electron.* 39, 1555-1565 (2003).

[13]   J. Scheuer and A. Yariv, " Two-dimensional optical ring resonators based on radial Bragg resonance" *Optics Lett*. Vol. 28, No. 17 (2003)

[14]   J. Scheuer and A. Yariv, " Annular Bragg defect mode resonators " *Opt. Soc. Am. B.* Vol. 20, No. 11 (2003)

[15]   J. Scheuer and A. Yariv, " Circular photonic crystal resonators" *Physical Review E* 70, 036603 (2004).

[16]   D. Chang, J. Scheuer and A. Yariv, " Optimization of circular photonic crystal cavities beyond coupled mode theory" *Optics Express*, Vol. 13, No. 23, 9272-9279 (2005)

[17]   Jiří Chaloupka, Javad Zarbakhsh, and Kurt Hingerl, " Local density of states and modes of circular photonic crystal cavities " *PHYSICAL REVIEW B* **72**, 085122. (2005)

[18]   M. Fujita and T. Baba, " Microgear laser " *Appl. Phys. Lett.* 80 , pp. 2051-2053 (2002)

[19]   K. Nozaki and T. Baba, " Quasiperiodic photonic crystal micro-cavity lasers "*Appl. Phys. Lett.* 84, pp. 4875-4877 (2004)